ON THE STRAIN IN SILICON NANOCRYSTALS

A THESIS
SUBMITTED TO THE DEPARTMENT OF PHYSICS
AND THE INSTITUTE OF ENGINEERING AND SCIENCE
OF BILKENT UNIVERSITY
IN PARTIAL FULFILLMENT OF THE REQUIREMENTS
FOR THE DEGREE OF
DOCTOR OF PHILOSOPHY

By
Dündar Yılmaz
June 2009

I certify that I have read this thesis and that in my opinion it is fully adequate, in scope and in quality, as a dissertation for the degree of doctor of philosophy.

Assoc. Prof. Ceyhun Bulutay (Supervisor)

I certify that I have read this thesis and that in my opinion it is fully adequate, in scope and in quality, as a dissertation for the degree of doctor of philosophy.

Prof. Tahir Çağın (Co-Advisor)

I certify that I have read this thesis and that in my opinion it is fully adequate, in scope and in quality, as a dissertation for the degree of doctor of philosophy.

Assoc. Prof. Oğuz Gülseren

I certify that I have read this thesis and that in my opinion it is fully adequate, in scope and in quality, as a dissertation for the degree of doctor of philosophy.

Prof. Raşit Turan

I certify that I have read this thesis and that in my opinion it is fully adequate, in scope and in quality, as a dissertation for the degree of doctor of philosophy.

Assist. Prof. Emrah Özensoy

Approved for the Institute of Engineering and Science:

Prof. Mehmet Baray,
Director of Institute of Engineering and Science

Abstract

ON THE STRAIN IN SILICON NANOCRYSTALS

Dündar Yılmaz
PhD in Physics
Supervisor: Assoc. Prof. Ceyhun Bulutay
June 2009

In this Thesis we present our achievements towards an understanding of atomistic strain mechanisms and interface chemistry in silicon nanocrystals. The structural control of silicon nanocrystals embedded in amorphous oxide is currently an important technological problem. First, our initial attempt is described to simulate the structural behavior of silicon nanocrystals embedded in amorphous oxide matrix based on simple valence force fields as described by Keating-type potentials. Next, the interface chemistry of silicon nanocrystals (NCs) embedded in amorphous oxide matrix is studied through molecular dynamics simulations with the chemical environment being governed by the reactive force field model. Our results indicate that the Si NC-oxide interface is more involved than the previously proposed schemes which were based on solely simple bridge or double bonds. We identify different types of three-coordinated oxygen complexes, previously not noted. The abundance and the charge distribution of each oxygen complex is determined as a function of the NC size as well as the transitions among them.

Strain has a crucial effect on the optical and electronic properties of nanostructures. We calculate the atomistic strain distribution in silicon NCs up to a diameter of 3.2 nm embedded in an amorphous silicon dioxide matrix. A seemingly conflicting picture arises when the strain field is expressed in terms of bond lengths versus volumetric strain. The strain profile in either case shows uniform behavior in the core, however it becomes nonuniform within 2-3 Å distance to the NC surface: tensile for bond lengths whereas compressive for volumetric strain. We reconcile their coexistence by an atomistic strain analysis.

Vibrational density of states (VDOS) affects the optical properties of Si-NCs. VDOS obtained by calculating velocity autocorrelation function (VACF) using velocities of the atoms is extracted from the molecular dynamics simulations. The information on bonding topology enables classification of atoms in the system with respect to their neighbor atoms. With help of this information we separate contributions of different type of atoms to the VDOS. Calculating VACF of different type of atoms such as surface atoms and core atoms of nanocrystal, to the system facilitates understanding of the effects of strain fields and interface chemistry to the VDOS.

Keywords: silicon, nanocrystal, interface, strain, molecular dynamics, monte carlo, simulation, vibrational spectra

Özet

SİLİSYUM NANO ÖRGÜLERDE GERİLME HAKKINDA

Dündar Yılmaz
Fizik Doktora
Tez Yöneticisi: Doc. Dr. Ceyhun Bulutay
Haziran 2009

Bu Tez'de camsı silisyum dioksidin (a-SiO_2) içine gömülü silisyum nano örgülerin (Si-NÖ) atomik mekanizmalarının ve nano örgü (NÖ) oksit arayüzünün kimyasal özelliklerinin anlaşılmasına yönelik çalışmalarımızı sunuyoruz. Silisyum nano örgülerinin yapılarını belirleyebilmek çözülmeyi bekleyen önemli bir teknolojik problemdir. Bu amaçla, başlangıç olarak silisyum nano örgülerin oksit içinde tavlama sırasında oluşumunu modelledik. Ardından Si-NÖ/a-SiO_2 arayüzünün kimyasını anlamak için, benzetim sırasında kimyasal reaksiyonları da modelleyebilen bir potansiyel kullanarak moleküler dinamik (MD) benzetimleri yaptık. Sonuçlarımız Si-NÖ/a-SiO_2 arayüzünün sanıldığı gibi çift bağ ya da köprü bağ yapan oksijenlerden oluşmadığını bunun yanında, NÖ yüzeyinde üç bağlı oksijen komplekslerin varlığını da gösterdi.

Gerilme nano yapıların optik ve elektronik özellikleri üzerinde önemli bir etkiye sahiptir. a-SiO_2 içine gömülü Si-NÖ'lerdeki gerilme dağılımını atomistik düzeyde hesapladık. Çapları 3.2 nm'yi bulan NÖ'lerde yaptığımız hesaplarda şaşırtıcı sonuçlar elde ettik. NÖ çekirdeğinde düzenli bir sıkışmayı hem bağ uzunluklarında hem de gerilme dağılımında gözlemlememize karşın, NÖ yüzeyinin hemen altındaki Si-Si bağları oksit atomlarının etkisi ile uzarken aynı bölgenin *sıkışma* şeklinde deforme olduğunu gözlemledik. Başta çelişkili gibi görünen bu iki sonuç, Si-NÖ'nün içine gömüldüğü a-SiO_2'in NÖ'yü düzensiz deforme ettiği gerçeği ile anlam kazanmaktadır. Bu düzensiz deformasyon sayesinde NÖ yüzeyinin hemen altında Si-Si bağları uzarken aynı bölgedeki gerilme dağılımı negatif karakterlidir.

Titreşimsel durum yoğunluğu (TDY) Si-NÖ'lerin optik özelliklerini etkiler. Çalışmamızda TDY, hız korelasyon fonksiyonu (HKF) hesaplanması yoluyla elde edildi. HKF ise MD benzetimi sonucunda elde edilen atomların hız bilgileri kullanılarak hesaplandı. Bunun yanında MD benzetimi sonucu elde ettiğimiz her atomun hangi atomlarla bağ yaptığı hakkındaki bilgi sistemdeki atomları sınıflandırmamıza olanak verdi. Bu sınıflandırmayı kullanarak geliştirdiğimiz 'Renkli-HKF' yöntemi ile sistemdeki farklı özelliklerdeki atomların TDY'na katkılarını ayrı ayrı değerlendirdik. Bu sayede Si-NÖ çekirdeğindeki silisyum atomları ile Si-NÖ yüzeyindeki silisyum atomlarının TDY'na yaptığı farklı katkıları birbirinden ayırt edebildik. Böylelikle gerilmenin ve Si-NÖ/a-SiO_2 arayüzü kimyasının TDY üzerindeki etkisini inceledik.

Anahtar sözcükler: silisyum, nano örgü, arayüz, gerilme, moleküler dinamik, Monte Carlo, benzetşm, titreşimsel durum fonksiyonu

Acknowledgement

First of all I would like to thank to the best person I have ever met, my thesis supervisor Prof. Ceyhun Bulutay. He guided me throughout this work with his wisdom and insight. He also became a role model for me with his great personality and kindness.

I would like to express my sincere appreciation to my thesis co-advisor Prof. Tahir Çağın for his guidance and inspirations.

I am grateful to the faculty members and the staff of the Physics Department of Bilkent University for providing a productive scientific environment throughout my studies.

I would like also to thank to my friends for their companion, support and friendship.

I would like to express my deeply gratitudes to my father Enver Yılmaz and my mother Fatma Yılmaz for providing me a home with full of love.

Finally I would like to thank to my soul mate Fatma İnce Yılmaz for her love, friendship, tender and endless support in my life.

To my wife

Contents

List of Figures

List of Tables

Now when I was a young boy, at the age of five
My mother said I was, gonna be the greatest man alive
Muddy Waters, "Mannish Boy",
Mannish Boy, Sony/BMG. 1955.

Chapter 1

Introduction

Silicon is the second most abundant element of the earth crust after oxygen. Because of its chemical and physical properties whole semiconductor industry is based on silicon. However, building optoelectronic devices is impossible with bulk silicon due to its indirect band gap. Towards the end of the 20^{th} century it became clear that properties of silicon change in the nanoscale in a way that these changes enable coupling visible light photons with electrons of silicon. Thus nano sized silicon based systems promise to the semiconductor industry the chance of low cost fabrication of interesting devices such as tunable lasers, light emitting diodes, non-volatile memories.

The physics of nano systems keeps its mystery in many aspects. One of the most crucial subjects to resolve is interaction of light with these systems. For the case of germanium or silicon nanoclusters, increase of band gap with decrease in radius of nanoclusters is related to the size effects by quantum confinement model. Photoluminescence measurements of silicon nanocrystals (Si-NCs) embedded in amorphous silicon dioxide (a-SiO_2) showed that band gap is not increased as much as the prediction of the quantum confinement model [1]. The interface between Si-NC and a-SiO_2 is thought to be responsible for this difference [1–3]. Especially double bonds [1] and bridge bonds [3] between oxygens of a-SiO_2 were blamed for the deviation from the quantum confinement model. However, there is no concencus among scientist on the understanding of physics of electron photon interaction in Si-NC embedded in a-SiO_2.

Another open issue is the strain. In continuum mechanics, the effect of strain on vibrational modes of a rigid body is well understood. As an example, one can tune the vibration frequency of a guitar string by changing its tension. Strain has direct effects on energy gaps [4] and phonon spectra [5] of Si-NCs. Several effects such as bond mismatch, thermal residual strain were proposed as possible sources of strain fields in Si-NCs. However mechanisms of these effects of strain are not fully explained. Thus strain state of Si-NCs embedded in a-SiO_2 is also a subject of debate. Strain is proposed as a tool to *tune* the optoelectronic properties of nano systems [6]. Since direct measurement of strain has not been achieved yet, an atomistic point of view to analyze strain fields in Si-NCs is needed to explain these mechanisms.

Vibrational density of states (VDOS) determines optical properties of Si-NCs. Understanding VDOS of Si-NCs is the first step in design of Si-NC based optical devices. Two aforementioned effects, strain and interface chemistry, to VDOS of Si-NCs can be directly explored using molecular dynamics simulation (MD) technique. With a reactive potential, MD simulation provides not only velocities of atoms, but also bonding information and positions of atoms.VDOS can be obtained by calculating velocity autocorrelation function (VACF). The information on bonding topology enables classification of atoms in the system with respect to their neighboring atoms. This allows extracting contributions of different type of atoms to the VDOS. Calculating VACF of different type of atoms such as surface atoms and core atoms of nanocrystal, facilitates the understanding of the effects of strain fields and interface chemistry to the VDOS. Thereby VACF can be the last piece of the puzzle of interaction of light with Si-NCs.

This Thesis is devoted to understanding of the atomistic mechanical properties and interface chemistry of Si-NCs embedded in a-SiO_2 using computational tools. The very first step that we present in Ch. 2, is to understand formation of Si-NCs in the a-SiO_2 during the annealing process. We use Monte Carlo simulation technique with an oxygen diffusion scheme [7]. We show the need of a more complex potential to represent the surface chemistry of Si-NCs. In Ch. 3 we present our main approach: We use a reactive force field with MD simulation scheme to understand the surface chemistry of Si-NCs. We show reaction pathways at the Si-NC/a-SiO_2. We also observe stretching of the Si-Si bonds just under the nanocrystal surface [8]. We reserve Ch. 4 for the presentation of our next task in which we analyze strain state of Si-NCs. In Ch. 5 we present details of the VACF calculation. Finally we demonstrate the technique called "Painted VACF" which we used to calculate contributions of different types of atoms to the VDOS. Our most important findings and conclusions are summarized in Ch. 6.

They say love is just a proposition people
It's strickly a game of give and take
Oh, I don't claim to be no gambler people
Oh, I dont' know much about the dice
B. B. King, "Gambler's Blues",
Great Moments with B. B. King, MCA Records 1980.

Chapter 2

Formation of Nanocrystal Silicon Embedded in Oxide

The contents of this chapter have partially appeared in:
Atomistic structure simulation of silicon nanocrystals driven with suboxide penalty energies*, D. E. Yılmaz, C. Bulutay and T. Çağın, Journal of Nanoscience and Nanotechnology* ***8****, 635 (2008).*

2.1 Introduction

In this part of the Thesis we describe our multilevel algorithm to simulate the formation of Si NC embedded in a-SiO_2. Our approach starts with the generation of a-SiO_2 with excess silicon so as to incubate Si NC formation. This part is based on the standard Wooten-Winer-Weaire (WWW) model [9]. Next, with a crucial insight from Burlakov *et al.* [10], the evolution of the silicon-rich-oxide towards an embedded NC is driven by the oxygen diffusion process, implemented in the form of a Metropolis algorithm based on the suboxide energies determined from *ab initio* computations [11]. This is followed by the shape constraints so as to attain a spherical geometry. The details of the approach and the results are provided in the following sections.

2.2 Valence Force Field Model

Suppose that we have a system at its equilibrium. This means that net force on all atoms should be zero. Near this equilibrium, we can model interactions between atoms in the system as lossless springs attached between point masses. In this so-called harmonic regime, we assume that total internal energy of the system is elastic energy. E_{tot} which is a function of the positions of all of the atoms in the system:

$$E_{tot} = E_{tot}(0) + \sum_i \frac{\partial E_{tot}}{\partial u_i} u_i + \frac{1}{2} \sum_{i,j} \frac{\partial^2 E_{tot}}{\partial u_i \partial u_j} u_i u_j. \tag{2.1}$$

All first derivatives of energy should vanish since they are evaluated at equilibrium and second derivatives give spring constants that we model the interaction of atoms in the system. In principle, to calculate all of these modes from the theory of electronic structure gives the most accurate description of the system, which is equivalent to the calculation of all the force constants. This needs a lot of computation power even for a small system.

To work with larger systems, the number of independent parameters that defines the system must be reduced for a reasonable computation time. A simple such model for the diamond or zinc-blende structures is to assume that there exist only two-body ('bond-stretching') and three-body ('bond-bending') interactions in the system. In this approximation we can rewrite the Eq. 2.1 as:

$$E_{elastic} = \sum_{i,j}^{N_{bonded\ atoms}} \frac{1}{2} C_0 (\partial r_{ij})^2 + \sum_{i,j}^{N_{neighbor\ bonds}} \frac{1}{2} C_1 (\partial \theta_{ij})^2 \qquad (2.2)$$

where ∂r_{ij} term represents the deviations of the bond lengths and $\partial \theta_{ij}$ term represents deviations of the angle between adjacent bonds from the tetrahedral angle; first must be summed over all bonds and the latter must be summed over all adjacent-bond angles. In a more general form:

$$E_{elastic} = \sum_{i,j}^{N_{bonded\ atoms}} \frac{1}{2} C_0 (r_{ij} - r_{ij}^0)^2 + \sum_{i,j}^{N_{neighbor\ bonds}} \frac{1}{2} C_1 (\cos(\theta_{ij}) - \cos(\theta_{ij}^0))^2 \qquad (2.3)$$

where r_{ij}^0 and θ_{ij}^0 are equilibrium bond lengths and angles, respectively. This model, first proposed by Keating [12] is usually called *Keating Potential* or *The Valence Force Field Model* and requires much less computation power then *ab initio* calculations. On the other hand this model is accurate only near the equilibrium condition (i.e. elastic limit).

2.3 Generation of Amorphous Systems

2.3.1 Wooten-Winer-Weaire Method

The seminal work for the generation of amorphous systems was proposed by Wooten, Winer and Weaire (WWW) [9]. They used Keating potential [12] to describe the system where the total energy of system depends on the deviation of bond length and angles between adjacent bonds from the ideal crystal case. We store a list of bonded atoms during the simulations and ignore interactions of non bonded atoms. In this method, we start with a diamond crystal. Then we apply random bond switches as illustrated in Fig. 2.1 to erase crystal traces from the system. This corresponds to heating the system to its melting temperature. Next we relax the system using a Keating type potential with a slight modification

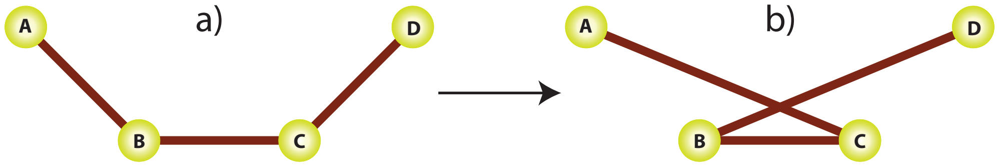

Figure 2.1: Illustration of bond switch used in WWW method. We brake bonds between atoms (a) A and B and C and D and create bonds between atoms (b) A and C and B and D

[13]. In fact we only update bond list with bond switches, since total energy is calculated through this bond list, during relaxation atoms will have new coordinates which lowers the total energy with respect to their bond topology. To reach an amorphous state we cool down the system using a Metropolis algorithm [14]. After each bond switch we relax the system and compare total energy of the system with before bond switch. If the total energy of the system is lowered with the bond switch we accept otherwise we reject it with a probability proportional to temperature of the system:

$$P = \min\left(1.0, e^{\frac{E_i - E_f}{kT}}\right) \tag{2.4}$$

where k is the Boltzmann's constant. We pick a random number r between 0 and 1, then if this number is less than P, then we accept this bond switch. If this random number is greater than P we reject the bond switch and return the system to previous state. To speed up the calculation we relax the system locally after every bond switch. We continue these bond switches while slowly decreasing the temperature. Total elastic energy of the system also decrease with temperature. At low temperatures we automatically accept bond switches which lower the total energy of the system and we mostly reject ones that increase the total energy of the system. In fact this algorithm is nothing but the simulated annealing in Monte Carlo (MC) scheme [15].

Another way to generate an amorphous system is to mimic annealing using Molecular Dynamics (MD) simulation technique. In MD simulation, for every time step positions and velocities of atoms at next time step are integrated using forces on atoms. These forces are calculated via first derivative of energy of the system which is defined by a chosen potential. In our case we use a reactive force field to define the energy of system [16]. To mimic annealing process we first increase the temperature of the system above its melting temperatures and slowly cool down the system. However MD technique has certain disadvantages. Typical MD step time for a reliable simulation is on the order of femto seconds (10^{-15}s). To simulate even for 1 s of the system evolution we need to calculate 10^{+15} MD steps. This brings an unreasonable computational budget. On the other hand MC method simulation goes on in probability domain rather than in time domain. Creating a clever MC algorithm will end up very fast and accurate results. Thus MC method is more efficient than MD method to simulate larger systems with processes that takes long times. We briefly discuss MD simulation technique in Ch. 3.

2.3.2 Modified Wooten-Winer-Weaire Method

Using WWW approach with a small modification one can generate a-SiO$_x$ or a-GeO$_x$ structures with a desired stoichiometry. As the first step, to generate amorphous silicon-rich-oxide we start with a 1000-atom diamond Si crystal. The energetics of the system is described by Keating-type two-body and three-body potentials with further addition of a repulsive potential between non-bonded atoms to prevent their overlap. Using WWW random bond transpositions, we generate a-Si system with 13° rms bond angle deviation of Si-Si-Si bonds and 0.3 Å rms bond length deviation of the Si-Si bonds. In the WWW method after each bond transposition the system is relaxed using conjugate gradient minimization scheme to decide whether to accept or reject the step based on a Metropolis algorithm.

The usual Boltzmann's factor derives the decision process. Since we start with an ideal crystal structure we need to erase the traces of the initial topology. This is achieved by randomizing the system by accepting all bond transpositions (i.e. temperature of system being set to infinity) till system reaches 23° rms bond

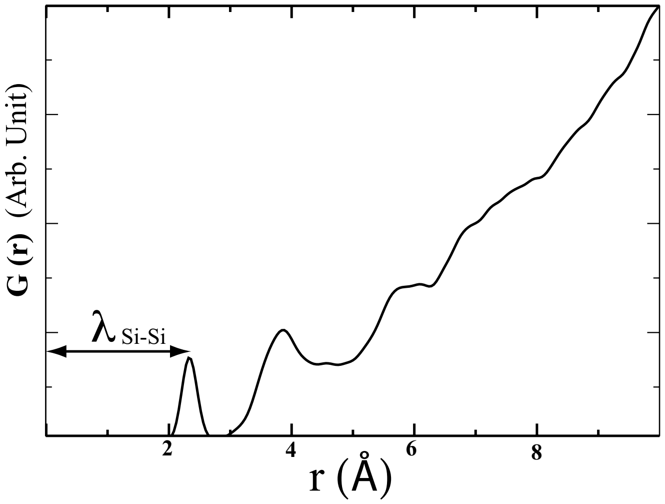

Figure 2.2: Radial distribution function of Si atoms. First peak resembles Si-Si bond length. Second peak's width indicates the rms bond angle deviation.

angle deviation for the Si-Si-Si bonds. After this point we set the temperature of system to kT=0.40 eV and continue random bond transpositions. In this way energy of system decreases and it cools down to an amorphous state with a desired rms bond angle deviation.

Radial distribution function is the main diagnostic tool to compare simulation results with experiment. In Fig. 2.2 we present graph of radial distribution function versus distance from a chosen atom in a-Si. First peak resembles mean bond length of Si-Si bonds while second peak's width resembles bond angle deviation of Si-Si-Si bond angle. After preparing the 1000-atom a-Si system we generate amorphous silicon-rich-oxide (i.e. SiO_x with $x < 2$) by randomly inserting required amount of oxygen atoms between Si atoms. After the insertion of oxygen atoms we expand the simulation box to acquire the correct density. Next, we relax the system using the conjugate gradient method. With this technique we end up with an amorphous silicon rich oxide with a desired Si to O ratio. Since we are dealing with Si-NC embedded in an amorphous matrix generating amorphous silicon dioxide is crucial to have a realistic medium.

2.4 Formation of Silicon Nanocrystals

Silicon-rich-oxide can be fabricated by the ion implantation method [17]. After implanting silicon atoms into a-SiO_2, the system is baked at 700 K. At these temperatures, oxygen atoms diffuse and excess silicon atoms form the nanocrystals. The main driving factor for the oxygen diffusion is the energy difference between a silicon atom bonded to four oxygens and a silicon atom bonded to less than four oxygens. Based on *ab initio* calculations on small Si clusters representing non stoichiometric systems, Hamann showed that the energy of Si atoms varies with oxidation states [11]. This variation is referred to as 'suboxide penalty'. In such a system the suboxide penalty favors silicon atoms bonding with either four oxygen atoms or four silicon atoms. These energy differences force oxygen atoms to diffuse to fill up silicon atoms' bonds. Based on this fact Burlakov *et al.* modeled the phase separation of non stoichiometric amorphous silica [10]. They mapped Metropolis Monte Carlo simulations to simple rate equations thereby extracting the suboxides densities.

As the evolution of system is driven by the diffusion of oxygen atoms we implement the following Monte Carlo step illustrated in Fig. 2.3. In this Monte Carlo (MC), step first a silicon atom with oxidation state between 1 to 3 is randomly chosen, then one of oxygen neighbors of this silicon atom is transferred to the midpoint of Si-Si bond of this silicon. Difference of the initial and final suboxide energies of system is used in the decision of the step. The temperature parameter for this step is taken as kT=0.15 eV. Since oxygen diffusion is much slower than the relaxation process we assume that system is fully relaxed during this step. This assumption accelerates evolution of system. After 10^6 MC diffusion steps which are carried out in less than two hours with a standard computer, the excess silicon atoms start forming nanoclusters.

2.4.1 Shape of Nanocrystals

A silicon suboxide complex, denoted by Si(i) is defined as a silicon atom bonded with i oxygens. Since Si(1) and Si(2) atoms lie at the surface of NC while Si(3)

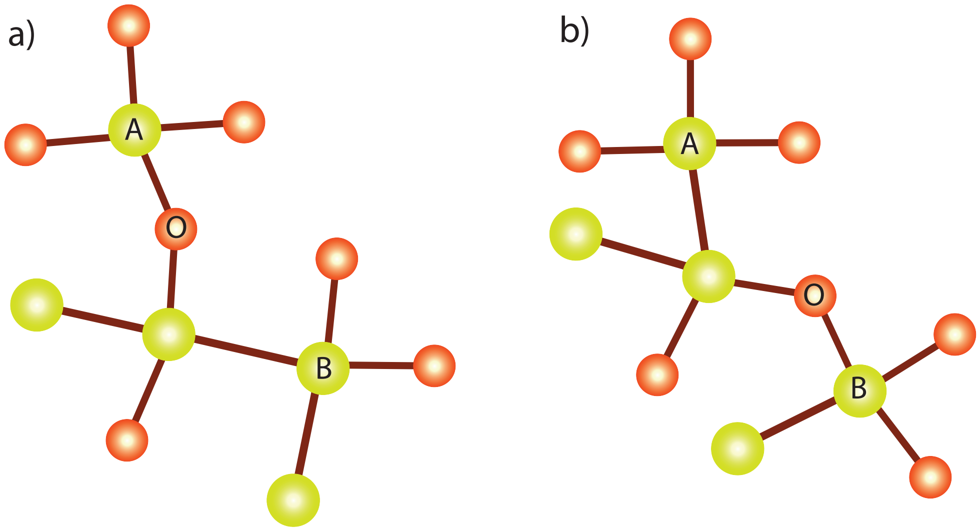

Figure 2.3: Illustration of the oxygen diffusion steps: Large spheres represent silicon atoms, small spheres represents oxygen atoms. In (a) oxidation state of atom A and atom B is 4 and 1, respectively. After the oxygen diffusion (b) oxidation state of atom A is decreased to 3 while oxidation state of atom B is increased to 2.

atoms lie mainly in the oxide region, densities of the suboxides determine the shape of the NC. In other words, suboxide energies play the most important role in the determination of the shape of the NC. In our simulation, the use of suboxide energies calculated by *ab initio* methods [11] results in a toroid-like shaped NCs (cf. Fig. 2.4). However TEM images show that Si NCs are sphere-like [18]. This situation forced us to modify suboxide energies to end up with sphere-like NC. To modify suboxide energies we use Burlakov's rate equation approach [10]. First, we calculate suboxide densities in the sphere-like NC by preparing an “ideal” NC embedded in a-SiO_2 by deleting oxygen atom in an a-SiO_2 system within a given radius [19]. Then using Burlakov's rate equation we fit suboxide energies to achieve suboxide densities calculated from the the “ideal” NC. However modifying suboxide energies was not enough to force the system to form sphere-like NC, instead we end up with cylinder-like NCs as shown in Fig. 2.5.

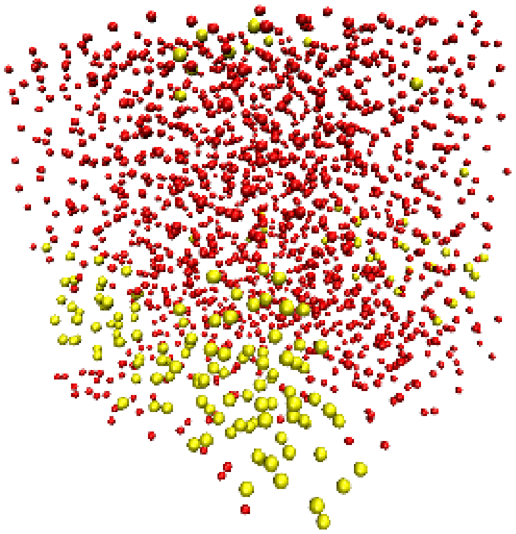

Figure 2.4: Snapshot of simulation, using suboxide energies from Ref. [11], after steady-state is reached. Only oxygen atoms (dark colored) and zero-oxidation-state silicon atoms (bright colored) are shown. Periodic boundary conditions are imposed around the simulation box.

A quantitative assessment of NC shape can be achieved by diagonalizing the shape tensor of the NC. The shape tensor of the NC is given by [20]:

$$G_{ij} = \frac{1}{N}\sum_{n=1}^{N}(r_{in} - R_i)(r_{jn} - R_j)\,, \tag{2.5}$$

where N is the number of NC atoms, R_i's are the coordinates of the center-of-mass of the NC and r_{in} is the ith coordinate of n'th NC atom. The ratio of three eigenvalues of shape tensor g_1, g_2 and g_3 (in descending order) determine the shape of the NC. Deviation from a perfect sphere (asphericity) is parametrized as:

$$\delta = 1 - 3\frac{I_2}{I_1^2}\,, \tag{2.6}$$

by Gaspari and Rudnick [21]. In Eq. 2.6 $I_1 = g_1+g_2+g_3$ and $I_2 = g_1g_2+g_2g_3+g_1g_3$ are the respective invariants of the shape tensor. For a perfect sphere eigenvalues of the shape tensor are equal so that the asphericity parameter is equal to zero.

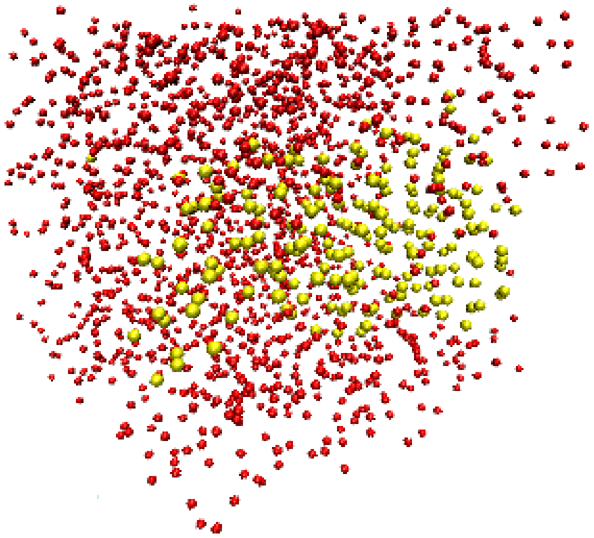

Figure 2.5: Snapshot of simulation using modified suboxide energies after steady state reached. Only oxygen atoms (dark colored) and zero-oxidation-state silicon atoms (bright colored) are shown. Periodic boundary conditions are imposed around the simulation box.

The asphericity parameter for NC formed using *ab initio* suboxide energies (Fig. 2.4) is 0.40 while for the NC formed using modified suboxide energies (Fig. 2.5) it becomes 0.23. So these NCs deviate too much from perfect sphere. Since surface to volume ratio is minimum for a sphere we also calculate the ratio of number of surface atoms to number of NC atoms for these NC. This ratio was also much larger than the 'ideal' NC case.

From these observations we conclude that such an approach still undermines the surface tension effects. On the other hand inclusion of asphericity parameter and surface-to-volume ratio can lead to better results. In our simulation with the modified suboxide energies, after the steady state is reached, we continue with MC steps but this time we include asphericity parameter and the surface-to-volume ratio to Metropolis decision. Inclusion of these parameters results in the formation of NC with asphericity parameter less than 0.001 and also g_1/g_2 falls in the range 1.0-1.1 and g_1/g_3 falls in the range 1.1-1.3. This means that inclusion of asphericity parameter and the surface-to-volume ratio yields almost spherical NC as illustrated in Fig. 2.4.1.

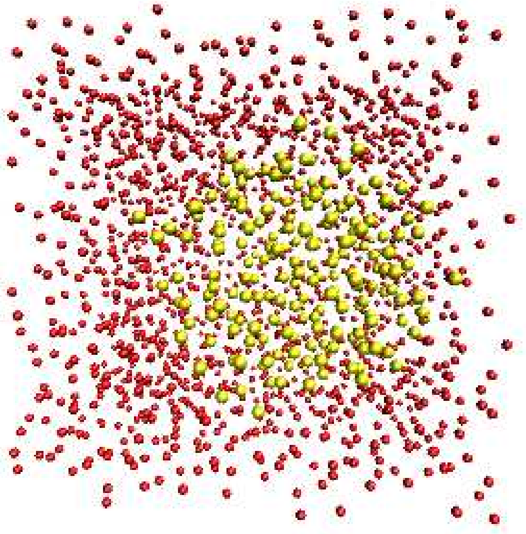

Figure 2.6: Snapshot of simulation using modified suboxide energies together with shape constraints, after steady state is reached. Only oxygen atoms (dark colored) and zero-oxidation-state silicon atoms (bright colored) are shown. Periodic boundary conditions are imposed around the simulation box.

The radial distribution function also gives important knowledge about size and shape of the NC. In Fig. 2.7 we present the radial distribution function of Si atoms with zero-oxidation state. First peak in this graph resembles mean bond length of Si-Si bonds in the NC region while width of second peak resembles deviation of Si-Si-Si angles from diamond crystal state. Also radius and diameter of the NC can be read from Fig. 2.7 since the probability of finding a pair with distance equal to radius is maximum and the probability of finding a pair within diameter distance is minimum in sphere-shaped NC. So from Fig. 2.7 we can extract the radius of NC as: $r_{NC} = 11.3$ Å.

The radial distribution function of Si atoms with zero-oxidation state to four-oxidation state is presented in Fig. 2.8. From this graph, width of the interface region between NC and oxide can be extracted. Since there is no pair with

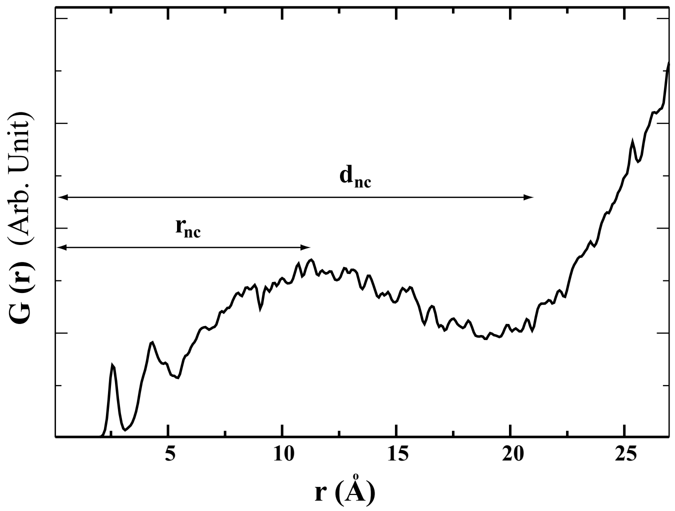

Figure 2.7: Radial distribution function of nanocrystal Si atoms. First peak resembles Si-Si bond length in the nanocrystal.

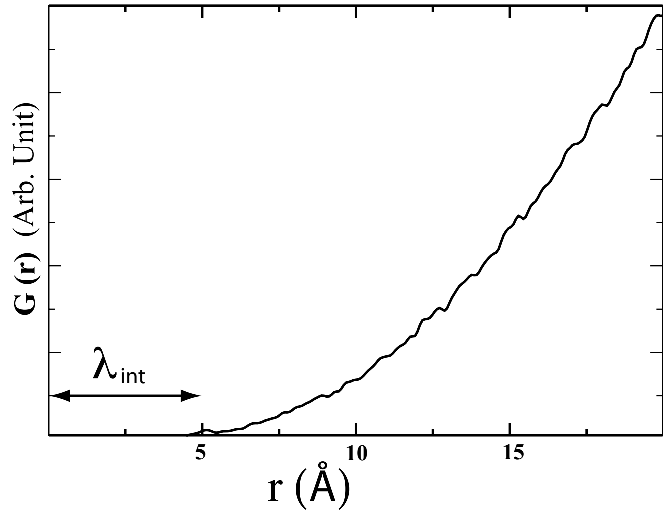

Figure 2.8: Radial distribution function of Si atoms with zero oxidation state to four oxidation state. Minimum distance between a Si atom with zero oxidation state and a Si atom with four oxidation state gives the width of interface region.

distance less then 4.2 Å we conclude that width of the interface region is about 4.2 Å. Once the interface regions are also accounted our predictions for the NC size as a function of oxygen molar fraction match reasonably well with the experimental data [10].

2.5 The Lessons Learned

In this part of the Thesis we tried to understand NC formation in amorphous silicon-rich-oxide using MC simulation technique with a Keating like potential and suboxide energies. We showed that these are models are not capable of defining system accurately especially the surface of the NC. This motivated us to use Molecular Dynamics simulation technique with a more complex force field to explore the dynamics of surface of silicon nanocrystals. In the next chapter we briefly introduce two main tools; MD simulation technique and the reactive force fields.

Did you see the lights
As they fell all around you
Did you hear the music
Serenade from the stars
Steve Miller Band, "Serenade",
Fly Like an Eagle, Capitol. 1976.

Chapter 3

Exploring Surface Chemistry of Silicon Nanocrystals Embedded in Amorphous silica matrix

The contents of this chapter have partially appeared in:
***Pathways of bond topology transitions at the interface of silicon nanocrystals and amorphous silica matrix**, D. E. Yılmaz, C. Bulutay and T. Çağın, Physical Review B.* ***77**, 155306 (2008).*

3.1 Introduction

After a long arduous effort, photoluminescence from silicon has been achieved from its nanocrystalline form [22]. A critical debate, however, continues over the nature of the interface chemistry of silicon nanocrystals (Si-NCs) embedded in amorphous silica which has direct implications on the optical activity of the interface [1–3, 23, 24]. Wolkin *et al.* reported that the oxidation of porous silicon quantum dots results in a red shift in the photoluminescence (PL) spectra which indicates the importance of oxygen-related interface bond topology [1]. Along this line, Puzder and co-workers compared PL calculations of nanoclusters with different passivants and surface configurations and proposed the main reason for the red shift to be double Si=O bonds [2]. Countering this, Luppi *et al.* reported excitonic luminescence features caused by Si-O-Si bridge bonds at the surface of silicon nanoclusters [3]. As a supporting evidence for the latter, Gatti *et al.* recently demonstrated that Si-O-Si is the most stable isomer configuration [23]. To reconcile, Vasiliev *et al.* claimed that bridge bonds and double bonds have similar effect on PL [24].

All of the work cited above represent density functional theory (DFT)-based calculations with small Si clusters of less than 100 atoms surrounded by either passivants like hydrogen [2, 3, 23] or oxygen [1, 2]. But actual samples are profoundly different: the fabricated systems consist of Si-NC with a diameter larger than 1 nm, embedded in *amorphous* silica (a-SiO_2) matrix. We use MD simulation technique with a reactive force field [16] to explore interface chemistry of Si-NCs embedded in silica matrix. In this chapter of the Thesis we present details and results of these simulations.

3.2 Simulation Environment

In Ch. 2 we described our first efforts to understand formation of silicon nanocrystals (Si-NCs) in the silicon-rich-oxide. We used a Monte Carlo technique to simulate system in probability domain. The idea is instead of calculating forces and velocities just to calculate the probability of the “MC-step” to occur and decide it via picking a random number. With such a technique one is limited with predefined “MC-steps”, but this limitation prevents us to focus on chemistry of NC surface which determines the optical activity of the system [1]. In this section we describe our simulation environment which enables us to understand dynamics and chemistry of the system. We divided this section into three subsections: First we briefly summarize basics of MD simulation technique. This part is based on the book by Frenkel and Smit [14]. Then we present the reactive force field approach [16] developed by Adri *et al.* which enables chemical reactions during the simulation. Finally we describe the method called “Delaunay Triangulation” that we use to define nanocrystal surfaces.

3.2.1 Basics of Molecular Dynamics Simulations

The word *simulation* means:

- The technique of imitating the behavior of some situation or process (whether economic, military, mechanical, etc.) by means of a suitably analogous situation or apparatus, especially for the purpose of study or personnel training [25].
- The imitative representation of the functioning of one system or process by means of the functioning of another [26].

and originates from the 17^{th} century Latin word *similis* which means *like* or *similar*. Imitating a system starts with writing the equations or constraints that governs the system. In the case of MD simulations these are equations of motion $\mathbf{F_i} = m_i\mathbf{a_i}$ for every atom i in the system. The idea is if we *imitate* interactions between atoms in a molecular system, we can determine the positions and velocities of atoms in the next step. We use the word *imitate* because interactions of atoms are too complex to formulate, instead we always model these interactions as simpler equations to understand the dynamics of the system. Suppose that, $U_i(\mathbf{r})$ is the interaction energy of atom i in the system. The net force on this atom is:

$$\mathbf{F_i} = -\nabla U_i. \tag{3.1}$$

We can write the position of atom i at around time t using Taylor expansion [14]:

$$\mathbf{r(t+\Delta t)} = \mathbf{r} + \frac{\partial \mathbf{r}}{\partial t}\Delta t + \frac{\partial^2 \mathbf{r}}{\partial t}\frac{\Delta t^2}{2} + \frac{\partial^3 \mathbf{r(t)}}{\partial t^3}\frac{\Delta t^3}{3!} + \vartheta(\Delta t^4) \tag{3.2}$$

or

$$\mathbf{r(t+\Delta t)} = \mathbf{r} + \mathbf{v(t)}\Delta t + \frac{\mathbf{F}\Delta t^2}{2m} + \frac{\partial^3 \mathbf{r(t)}}{\partial t^3}\frac{\Delta t^3}{3!} + \vartheta(\Delta t^4) \tag{3.3}$$

similarly we can write:

$$\mathbf{r(t-\Delta t)} = \mathbf{r} - \mathbf{v(t)}\Delta t + \frac{\mathbf{F}\Delta t^2}{2m} - \frac{\partial^3 \mathbf{r(t)}}{\partial t^3}\frac{\Delta t^3}{3!} + \vartheta(\Delta t^4) \tag{3.4}$$

adding these two equations:

$$\mathbf{r(t+\Delta t)} + \mathbf{r(t-\Delta t)} = 2\mathbf{r(t)} + \frac{\mathbf{F}\Delta t^2}{2m} + \vartheta(\Delta t^4). \tag{3.5}$$

The term Δt corresponds to the MD step which represents the free flight between two consecutive force updates. We can write the position of an atom at next MD step $t = t + \Delta t$ by using position at present and previous time step by rewriting Eq. 3.5:

$$\mathbf{r(t+\Delta t)} = 2\mathbf{r(t)} - \mathbf{r(t-\Delta t)} + \frac{\mathbf{F}\Delta t^2}{2m} + \vartheta(\Delta t^4). \tag{3.6}$$

This scheme to calculate positions at next MD step is called *Verlet Algorithm* [14]. The error term $\vartheta(\Delta t^4)$ in Eq. 3.6 depends on fourth power of MD time step. Choosing a small Δt will result in more accurate results and more calculations for a simulation that spans a constant amount of time. Velocities of atoms are not used to calculate positions in the *Verlet Algorithm* but one can compute velocities using positions:

$$\mathbf{v(t)} = \frac{\mathbf{r(t+\Delta t)} - \mathbf{r(t-\Delta t)}}{2\Delta t}. \tag{3.7}$$

In a typical MD simulation program, for a every time step forces on every atom is calculated using a model which approximates interactions between atoms. Then using these forces and positions of the atoms in the previous and present time step, the positions of the atoms in the next time step is calculated. Then positions of atoms are updated. This loop is repeated for the desired amount. There is a small error which is proportional to Δt^4 for *Verlet Algorithm*. This small error makes impossible to predict an atom's exact position after too many MD steps. Nevertheless our aim is not to predict atoms positions. Instead we aim to simulate ensemble averages of some quantities of the system such as temperature, pressure, chemical potential etc. Positions of atoms in a simulation is bounded with a region called *simulation box*. In some cases periodic boundary conditions are applied to one or more dimensions of the simulation box. The number of atoms N during the simulation could be chosen as a constant. In micro canonical ensemble; number of atoms N, volume of the simulation box V, and total energy of the system E (NVE simulation) are constants of the simulation. In canonical ensemble; number of atoms N, volume of the simulation box V and temperature of the system T (NVT simulations) are constants of the simulation. There are also other ensembles such as NPT or μVT. Temperature is defined as the average kinetic energy of the system, for a three dimensional system temperature is:

$$T = \frac{1}{3k_B} m \langle v^2 \rangle \tag{3.8}$$

There are various schemes to control temperature of the system constant which are called *thermostats*. We use Nose-Hoover thermostat to carry out NVT simulations [14]. There are also schemes to control total internal pressure of the system constant which are called *barostats* [14] however these schemes are not of interest for this Thesis.

3.2.2 Reactive Force Field: ReaxFF

In a MD simulation most of computational work is done during force calculation. Total computational workload depends on the model that is used to define interactions between atoms. In Ch. 2 we describe *Valence Force Field Model* which is one of the simplest model to describe covalently bonded systems. The need for a more complex model explained in last section of Ch. 2. For this purpose we use a reactive force field (ReaxFF) developed by Adri v. Duin *et al* [16]. In

ReaxFF, total energy of the system is divided into several partial energy terms:

$$E_{system} = E_{bond}+E_{over}+E_{under}+E_{lp}+E_{val}+E_{pen}+E_{tors}+E_{conj}+E_{vdWaals}+E_{Coulomb}. \tag{3.9}$$

In Eq. 3.9, E_{bond} represents bonding energy, E_{over} and E_{under} represent over coordination and under coordination energies, E_{lp} represents energy of lone electron pairs. The terms $E_{vdWaals}$ and $E_{Coulomb}$ represent non bonded van der Waals and Coulomb interactions. Unlike many other force fields, ReaxFF does not use implicit bond list to calculate chemical bond energy of the system. Instead bond order which determines the bond energy of the system calculated using local geometry i.e. distance between atoms, of the system and updated during the simulation [16]:

$$BO'_{ij} = BO'^{\sigma}_{ij} + BO'^{\pi}_{ij} + BO'^{\pi\pi}_{ij} \tag{3.10}$$

where BO'^{σ}_{ij}, BO'^{π}_{ij} and $BO'^{\pi\pi}_{ij}$ are represent uncorrected *sigma*, *pi* and *double pi* bond orders between atom i and atom j. These uncorrected bond orders are calculated using inter atomic distance r_{ij} between atom i and j:

$$BO'_{ij} = \exp\left[p_{bo,1}\left(\frac{r_{ij}}{r_0^{\sigma}}\right)^{p_{bo,2}}\right] + \exp\left[p_{bo,3}\left(\frac{r_{ij}}{r_0^{\pi}}\right)^{p_{bo,4}}\right] + \exp\left[p_{bo,5}\left(\frac{r_{ij}}{r_0^{\pi\pi}}\right)^{p_{bo,6}}\right] \tag{3.11}$$

After calculation of uncorrected bond orders for all atoms in the system, these bond orders are corrected by considering under/over coordination of atoms. Bond energy between atom i and atom j is calculated using bond orders:

$$E_{bond} = -D_e^{\sigma} BO^{\sigma}_{ij} \exp\left[p_{be,1}(1 - BO^{\sigma}_{ij})^{p_{be,2}}\right] \tag{3.12}$$

Other terms in Eq. 3.9 that contribute to total energy of the system depend on inter atomic distance. Additional non bonded interactions van der Waals and Coulomb interactions are also included in this force field. Charges of atoms are calculated in a classical way using electron equilibration method [27]. As a matter of fact the reactive force field (ReaxFF) model developed by van Duin *et al.* which improves Brenner's reactive bond order model [28] to a level of accuracy and validity allowing MD simulations of the full reaction pathways in bulk [16].

The parameters for this force field were obtained from fitting to the results of *ab initio* calculations on relevant species as well as periodic boundary condition DFT-based calculations of various crystalline polymorphs of relevant materials. The ReaxFF calculates bond orders which is the measure of bond strength from local geometry. This allows realistic chemical environment such as over/under coordination and bond breaking/formation for large-scale (about 5000 atoms) MD simulations.

3.2.3 From Points to Surface

Experimental works indicate that oxygen bonds at the nanocrystal surface determines optical activity [1, 3, 23, 24]. Suppose that we cut out a spherical silicon nanocrystal with diameter 2.0 nm from bulk (Fig. 3.1-a). Such a nanocrystal contains about 200 atoms. Although we cut a sphere from bulk crystal if we look closely we see that the surface of nanocrystal is not a sphere. In Fig. 3.1-b we also present the surface of this nanocrystal constructed with Delaunay Triangulation for comparison. If we compare Fig. 3.1-a with Fig. 3.1-b we observe that triangulated surface is a better definition for nanocrystal surface. Defining nanocrystal surface enables us to understand how distance to the surface effects bond lengths, strain, charges of atoms in the system. We also use same technique during inserting the nanocrystal into oxide matrix. For two dimensions, Delaunay Triangulation (DT) is creating triangles from a set of points such that no points in the set is inside the circumcircle of any triangle [29].

In three dimensions triangulation becomes creating tetrahedra from a set of points such that no points in the set is inside the circumsphere of any tetrahedron [29]. In this part of the Thesis we used a two dimensional DT [30]. Since our NCs are nearly spherical in shape, we triangulate projection points of surface Si atoms onto the unit sphere. Hence, we apply Delaunay triangulation over the two dimensional θ-ϕ plane. We can then create surfaces using this triangulation. Later on we shall start to use GEOMPACK in our analysis software to calculate DT in three dimensions [31].

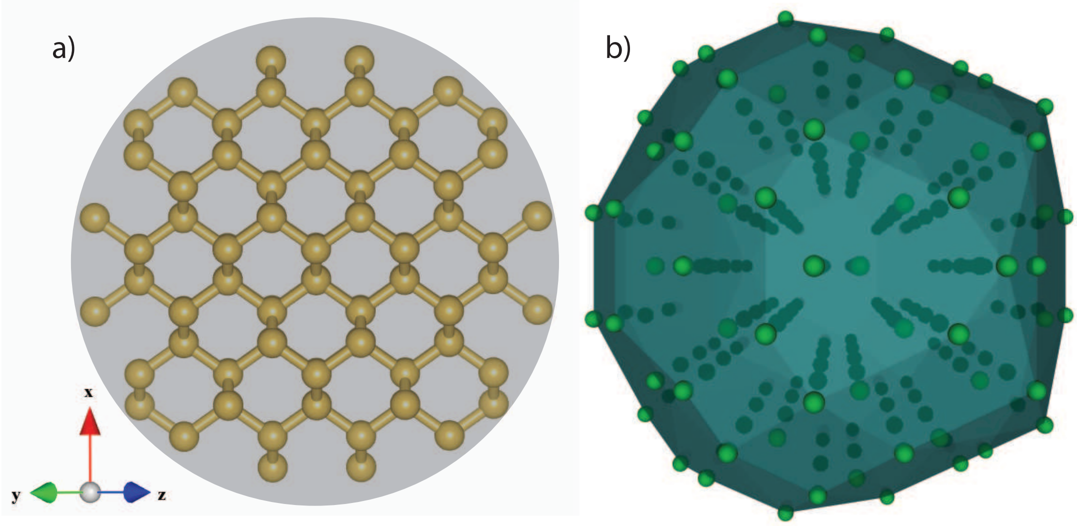

Figure 3.1: a) Nanocrystal with radius 1.0 nm cutted from bulk and (b) with its surface constructed by Delaunay Triangulation scheme.

3.2.4 The system

We use ReaxFF to represent the interactions in the model system. We start with a large simulation cell (box length 43 Å) of silica glass formed through a melting and quenching process used by Demiralp *et al.* [32, 33] to study silica glasses earlier. Next, similar to Hadjisavvas *et al.* [19], we delete all atoms within a predetermined radius to insert crystalline silicon to form NC. In this way, we create NCs with radii ranging from 5.5 Å to 16.7 Å. For the largest NC we insert 967 Si atoms into a spherical hole with radius 16.7 Å created in amorphous matrix. Even for this case, the minimum distance between NC surface to simulation box face is about 5 Å which can still accommodate the interface layer. We also pay special attention in the removal of spherical region so that the correct stoichiometry for the amorphous matrix is met. Thus, our amorphous matrix has two O atoms for every Si atom with a density of 2.17 g/cm^3 which is the density of glass at room temperature and atmospheric pressure.

We set periodic boundary conditions in all directions and while keeping NC at 100 K, we employ simulated annealing process to SiO_2 region to end up with an amorphous matrix free of artificial strain around the NC. Then we set whole systems' temperature to room temperature (300 K) and continue performing MD simulation for 75 ps to have thermal equilibrium between the two regions. We set MD simulation time step to 0.25 fs for all simulations. For every 62.5 fs time interval, we record the configurations to analyze the transitions taking place between different bond topologies.

3.3 Results and Discussions

To facilitate our discussion regarding the surface-bonded oxygen complexes, we distinguish among three different types of silicon atoms. We label those silicon atoms with all silicon neighbors each with zero oxidation state as c, to denote core silicon atom. Among the *remaining* (non-c) silicon atoms, those with at least one bond to c are labeled as s, denoting as a surface silicon atom. For further investigation of NC, we separate core Si atoms into two sub-categories as inner-core and outer-core atoms:

Among core Si atoms which have at least one surface Si neighbor categorized as outer-core Si atoms and rest of core Si atoms categorized as inner-core Si atoms. Finally, any other silicon atom is labeled as m, denoting matrix silicon atom. Hence, a complex consisting of an oxygen atom bonded with two surface silicon atoms is labeled as *ss*. The other oxygen complexes are *sm*, *ssm*, *sss*, *mms* as sketched in Fig. 3.2 where the last three correspond to three-coordinated oxygen (3cO) atoms. We separate this section into two subsections: In the first subsection we present effect of distance to the surface onto charge distribution, bond length strain and bond orders. In second subsection we present our works to reveal the chemistry of NC surface especially the role of 3cO's.

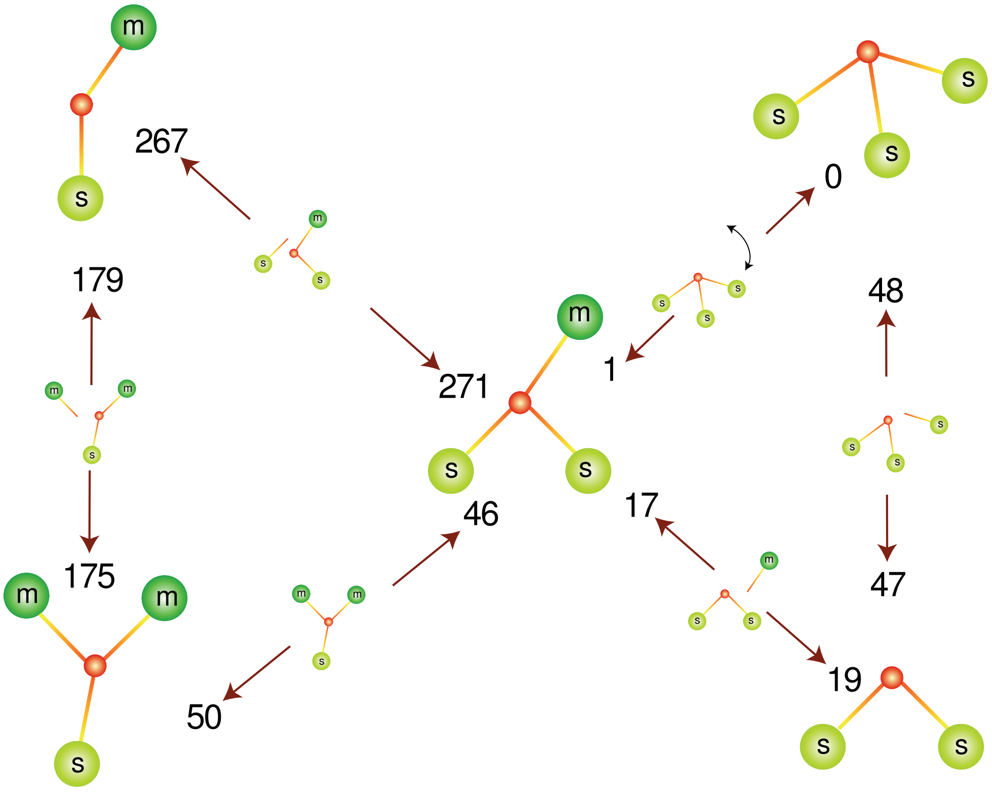

Figure 3.2: The transitions between different oxygen complexes bonded to the interface. Dark green (dark gray) large spheres represent matrix silicon atoms, and the light green (light gray) large spheres represents surface silicon atoms of the NC, small red (dark gray) spheres represent oxygen atoms. The numbers indicate the number of transitions recorded in the simulation in each direction among the complexes for the NC of radius 13.4 Å.

3.3.1 Surface Effects on Silicon Nanocrystal

To analyze surface effects on Si-NC, we construct NC surface using Delaunay triangulation scheme (Fig. 3.3 inset) [30]. This surface enables us to calculate every atoms' distance to NC surface. By this means we plot various data such as charge, bond order etc. with respect to distance to the surface, to extract information about surface chemistry of Si-NC embedded in amorphous matrix.

For different NC radii we observe similar trends in bond order distribution,

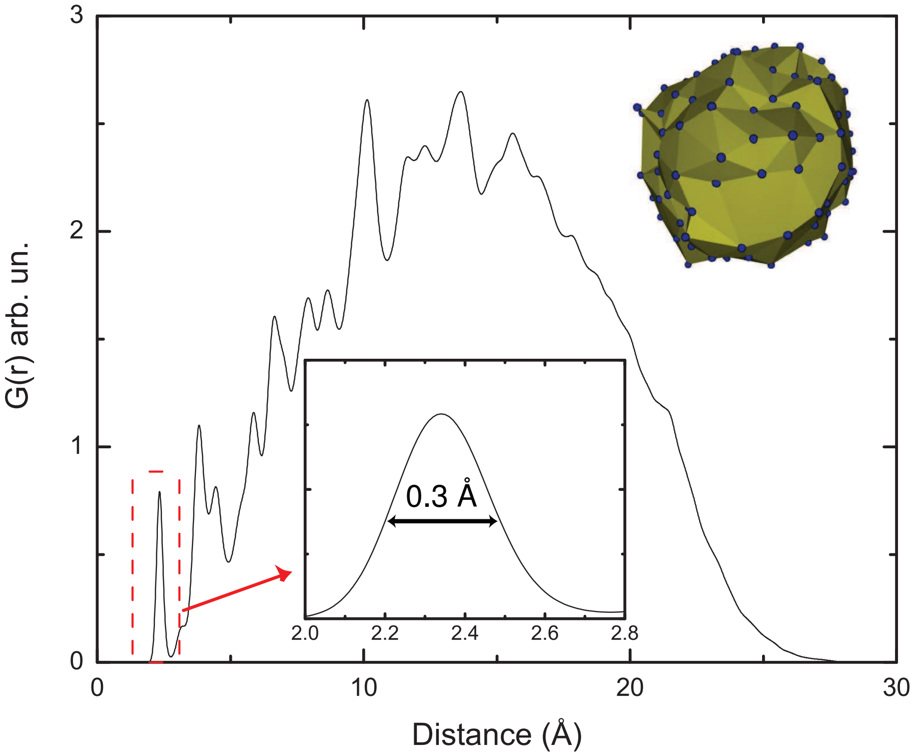

Figure 3.3: Radial distribution function of Si atoms in NC. Inset: First peak resembles Si-Si bond length distribution centered around 2.34 Å with 0.3 Å FWHM value. Second peak's width resembles bond angle deviation. Inset: Representation of NC surface created with Delaunay Triangulation. Blue dots represents surface silicon atoms.

average charges etc., therefore, we present only the figures of the system for a typical NC of radius 13.4 Å. A useful data to elucidate the structure of these systems is the radial distribution function (RDF). In Fig. 3.3 we present RDF of NC atoms only, where the first broad peak centered around 2.34 Å with a 0.3 Å full width at half maximum value (FWHM), represents Si-Si bond length distribution in NC (Fig. 3.3 inset). The maximum extent of the NC can also be read from same plot at about 27 Å, where the RDF goes to zero. Observation of a broad first peak at Fig. 3.3 demands further investigation of Si-Si RDF of NC atoms. For this purpose, in Fig. 3.4 we present bond length probability distributions (akin to RDF) for three categories of Si atoms: inner core (with no bonds to surface atoms), outer core (bonded to surface) and surface NC atoms. We observe from Fig. 3.4 that Si-Si bond lengths in the inner core are centered around the equilibrium value and have a narrow width due mainly to thermal vibrations, whereas the bond length distributions of outer core and surface atoms have increasing shift for the most probable bond length values and broader widths. These shifts and particularly the increase in distribution widths cannot be attributed to thermal broadening. Taken together these two observations is a clear indication of increasing strain as a function of distance from the center of the NC. To further investigate this deviation of Si-Si bonds from crystalline Si, in Fig. 3.5 we present bond length distribution with respect to distance to NC

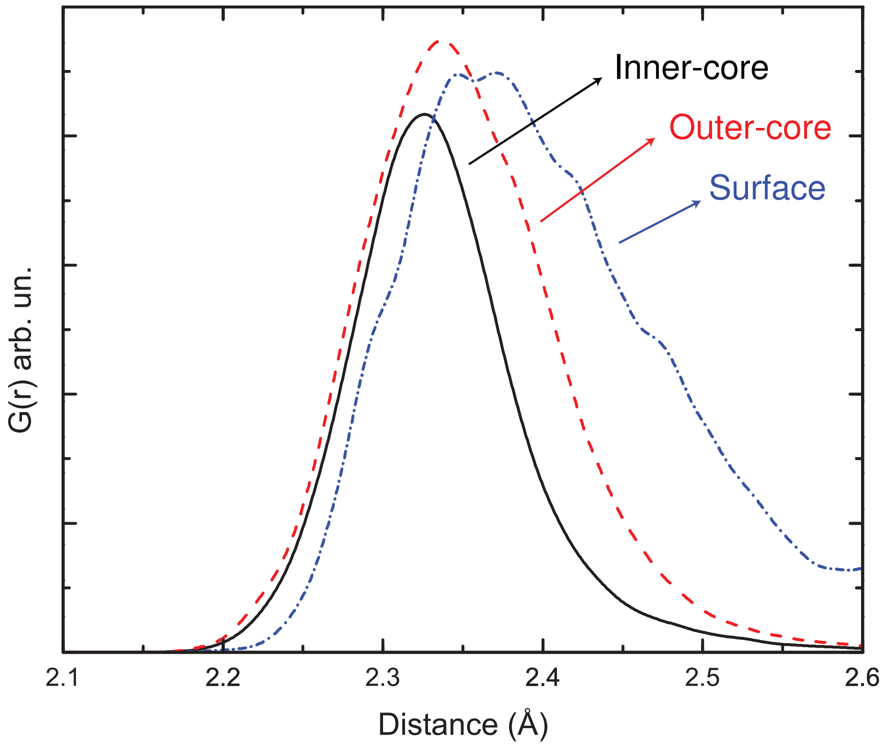

Figure 3.4: Bond distance probability distribution of Si atoms in NC. Solid line represents inner core Si-Si bonds, dashed line outer core Si-Si bonds, and dotted line represents the surface Si-Si bonds.

surface averaged over 2 ps of simulation time after the steady state is reached. This figure illustrates the gradual development of radial strain from the center to NC surface. These observations show clearly that oxidation at the surface of NC results in a tensile strain at Si-Si bonds which becomes significant only around the interface, while keeping the inner core almost unstrained. This tensile strain in the NC agrees with previous measurement of Hofmeister *et al.* [34].

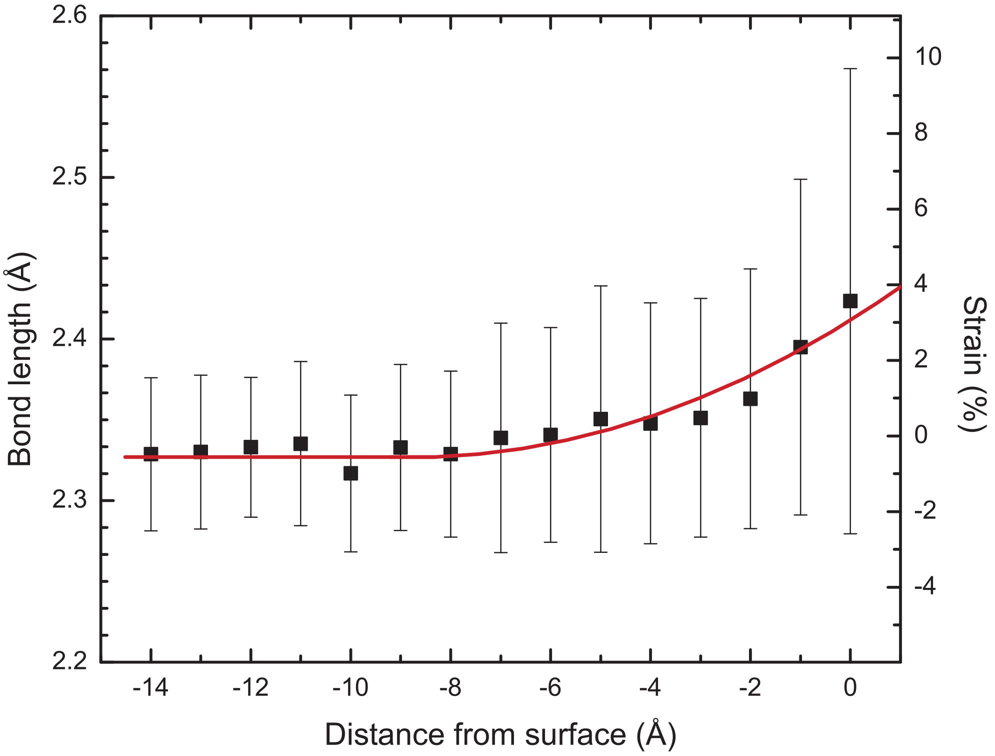

Figure 3.5: Variation of Si-Si bond length averages (calculated over 1 A wide bins) as a function of distance from the NC surface -which is defined by Delaunay tessellation. The solid line is a fit to the data to guide the eye.

Another consequence of this tensile strain is that the total bond orders of core-NC atoms are somewhat smaller than those of oxide-Si's as seen in Fig. 3.6. In the same figure we also show the calculated net charges using electron equilibration method [27]. Nearly zero net charges of the core-Si atoms reflects the covalent type of bonding well within the NC. The bonding becomes increasingly ionic

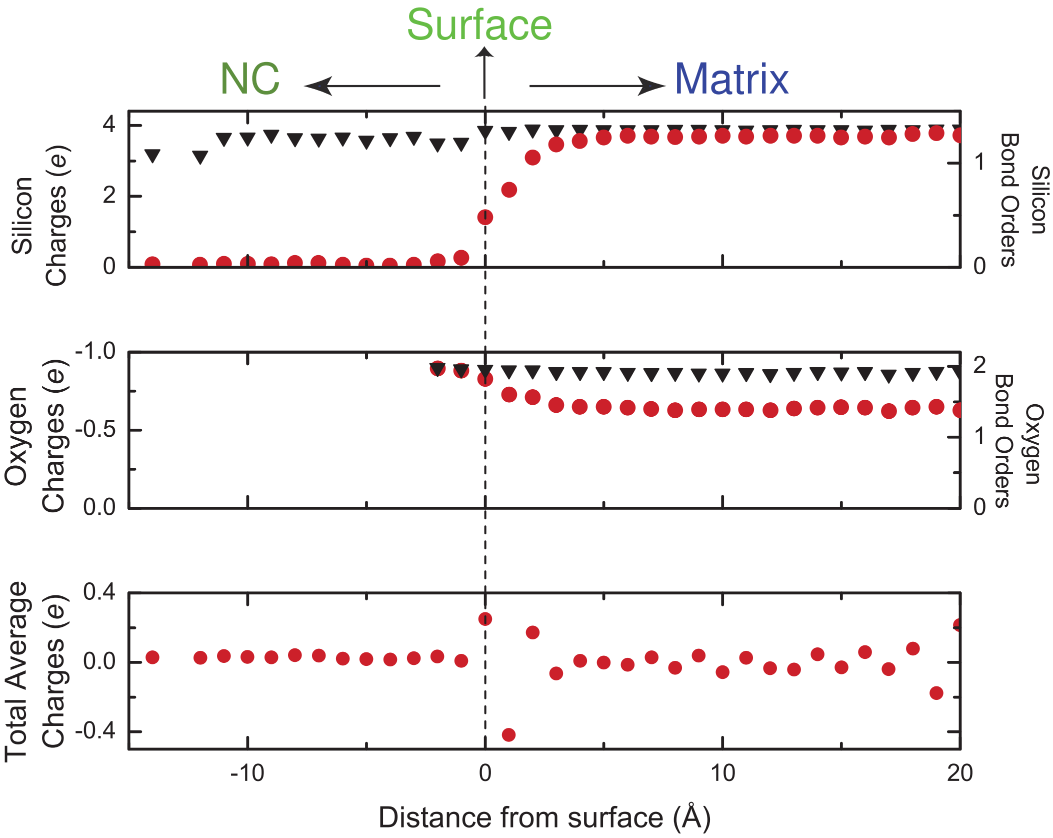

Figure 3.6: Top: Silicon bond orders (triangles) and charges (circles) as a function of distance from surface of NC; Middle: Oxygen bond orders and charges as a function of distance from the surface of NC; Bottom: Total average charge as a function of distance from the surface of NC. The averaging bin width is 1 Å.

away from the NC core as observed by the charges of Si atoms which reach the value of 1.3e at the oxide region (Fig. 3.6). As a result, the positive charges of surface-Si atoms form a shell at the surface of NC. This observation is similar with those obtained with DFT calculations [35, 36]. On the other hand, negative charges of oxygen atoms bonded to surface form another shell that enclose NC and finally total average charges approach to zero within the oxide region.

3.3.2 Surface Chemistry of Silicon Nanocrystals

In Fig. 3.6 we also observe that the magnitude of average charges of oxygen atoms which are bonded to surface are greater than those in the matrix. But, the bond orders are nearly the same. This is due to existence of 3cO atoms bonded to surface. Note that the average bond order of oxygen atoms which are bonded to surface is about two (cf., Fig. 3.6). Thus, those oxygen atoms form three partial bonds, two strong and one weak bond. Finally, we would like to note that unlike many others [1, 2, 24], we do not observe any double bonds.

The numbers attached to each arrow in Fig. 3.2 indicate the total number of registered transitions during the simulation in that direction between the complexes for a representative NC of radius 13.4 Å. Almost balanced rates in opposite directions is an assurance of the attainment of the steady state in our simulation. Note that we do not observe any direct transition other than the paths indicated in Fig. 3.2. For instance, a direct transition of the complex *ss* to *sm* does not take place, but it is possible through an intermediate transition over the *ssm* which is a 3cO. We should also remark that the balanced transitions continue to take place after the steady state is attained which indicates that the interface bond topology is dynamic, i.e. not frozen.

The occurrence of 3cO has been noted by a number of groups. Pasquarello showed that the bistable E_1' defect of α-quartz structure may lead to 3cO as a metastable state as well as Si-Si dimer bond and calculated the energy of the former to be higher than the latter. Pasquarello proposed that 3cO acts as an *intermediate metastable state* during structural relaxations at the interface [37]. Similarly Boero *et al.* observed 3cO atoms in their *ab initio* calculations [38] and reported this feature as a metastable state.

In Table 3.1 we present the collected statistical data at the end of the simulation of 75 ps. For all oxygen complexes, the number of bridges, average charges of bridge oxygens, and the average bridge angles for s-O-s are tabulated.

We observe in Table 3.1 that the number of *sss* complexes is very small due to narrow bond angle requirement of this configuration. For the remaining 3cO complexes, *ssm* and *mms*, their percentages are seen to increase with curvature.

This can explain the fact that other studies [37, 38] which have identified the 3cO complexes as metastable were based on the *planar* Si/SiO$_2$ interfaces. So, this is an indication of the importance of curvature in the stability of 3cO complexes. Hence, as one would expect, there is a linear relation between the total number of bridges with surface area as indicated in Fig. 3.7. This finding is supported by Kroll *et al.* who reported 3 and 33 such bridges for Si-NC with radii 4.0 Å and 7.0 Å, respectively [35].

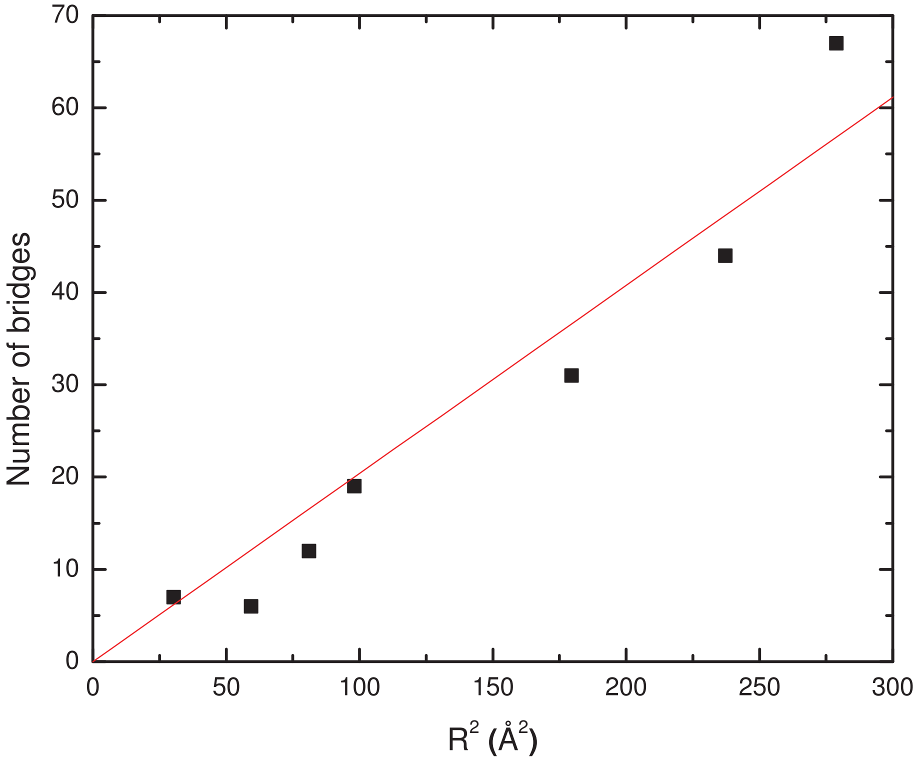

Figure 3.7: (Color online) The number of bridges at the Si-NC surface vs radius squared. The line is a linear fit to data.

Table 3.1: Statistical results of atom charges and numbers, N, for all NC diameters, D_{NC} considered. Abbreviations for atom types are explained in Fig. 3.2. Charges are in the units of electronic charge and the angles θ, are in degrees.

D_{NC}	N_c	N_s	N_O	ss			sm		ssm			sss		mms	
(Å)				N_{ss}	charge	θ_{ss}	N_{ss}	charge	N_{ssm}	charge	θ_{ss}	N_{sss}	charge	N_{mms}	charge
11.0	10	25	32	2	-0.88	169.7	24	-0.76	5	-0.74	97.0	0	—	1	-0.81
15.4	42	42	59	5	-0.77	136.1	51	-0.74	1	-0.73	82.7	0	—	2	-0.77
18.0	83	62	77	11	-0.82	120.5	56	-0.74	1	-0.83	141.2	0	—	9	-0.79
19.8	114	76	82	14	-0.82	139.3	49	-0.73	4	-0.81	123.1	1	-0.85	14	-0.79
26.8	353	143	170	20	-0.81	118.0	123	-0.74	11	-0.79	120.9	0	—	15	-0.76
30.8	558	203	243	35	-0.83	123.9	159	-0.74	10	-0.80	115.9	2	-0.80	34	-0.79
33.4	718	238	268	44	-0.83	123.0	179	-0.75	18	-0.80	125.7	4	-0.84	23	-0.78

There is no pain, you are receding.
A distant ships smoke on the horizon.
You are only coming through in waves.
Your lips move but I cant hear what youre sayin.
Pink Floyd, "Comfortably Numb",
The Wall, EMI. 1979.

Chapter 4

Strain Analysis of Silicon Nanocrystals

The contents of this chapter have partially appeared in:
***Analysis of strain fields in silicon nanocrystals**, D. E. Yılmaz, C. Bulutay and T. Çağın, Applied Physics Letters **94**, 191914 (2008).*

4.1 Introduction

The low dimensional forms of silicon embedded in silica have strong potential as an optical material [39]. Such heterogeneous structures inherently introduce the strain as a degree of freedom for optimizing their opto-electronic properties. It was realized earlier that strain can be utilized to improve the carrier mobility in bulk silicon based structures [6]. This trend has been rapidly transcribed to lower dimensional structures, starting with two-dimensional silicon structures [40]. Recently for silicon nanowires, there have been a number of attempts to tailor their optical properties through manipulating strain [41, 42].

For improving the optical and electronic properties of nanocrystals (NCs), the strain engineering has become an effective tool to be exploited [4, 43, 44]. A critical challenge in this regard is to analyze the strain state of the Si NCs embedded in silica. There still remains much to be done in order to understand strain in nanostructures at the atomistic level. Due to small density difference between Si NC and the surrounding a-SiO_2, a limited information can be gathered about its structure using transmission electron microscopy (TEM) or even high resolution TEM techniques [45]. Especially, molecular dynamics simulations with realistic interaction potentials present an opportunity, by providing more detailed critical information then the best imaging techniques currently available and clarify the analysis of experimental results.

Along this direction, previously [8] we focused on Si-Si bond length distribution and reported that Si-Si bond lengths are stretched upto 3% just below the surface of Si NCs embedded in amorphous SiO_2 which has also been very recently confirmed [46]. We also presented these results in Ch. 3. These stretched bonds forced us to work on strain analysis of silicon nanocrystals embedded in amorphous silicon dioxide. In this part of the Thesis we describe continuum and discrete strain formulation that we used to analyze strain fields and present our results.

4.2 Strain and Deformation

4.2.1 Continuum Strain Formulation

In continuum mechanics, relative positions of points in a body are changed when the body is deformed or strained. The strain is defined through this deformation. Continuum strain formulation that we present here is based on Ref. [47]. Before presenting strain formulation in continuum mechanics in three dimensions, for pedagogical purposes we first consider one dimensional deformation of a bar shown in Fig. 4.1). Left end of the bar is fixed to the wall and a force F is applied to the other end of the bar. The bar is deformed or strained as a result of applied force. Lets consider two points A and B on the bar before deformation occurs (Fig. 4.1-a). After deformation points A$_i$ and B$_i$ move to A$_f$ and B$_f$ respectively. Since point A$_i$ closer to the fixed end, point B$_i$ displaced more than point A$_i$ (Fig. 4.1-b). Distance between A$_i$ and B$_i$ before deformation was dx. After deformation distance between A$_f$ and B$_f$ is :

$$A_f B_f = dx + \frac{du}{dx}dx \tag{4.1}$$

If we define normal strain as the unit change in length in the direction of applied force is :

$$\epsilon_x = \frac{A_i B_i}{A_f B_f} = \frac{(du/dx)dx}{dx} = \frac{du}{dx} \tag{4.2}$$

We may extend this idea easily to derive strain formulation in three dimensions. Consider two points A and B on a three dimensional body. A$_i$ is at (x^0, y^0, z^0) and B is at (x, y, z). We assume that distance between A and B is infinitesimal. After the deformation point A displaces to $(x^0 + u_x^0, y^0 + u_y^0, z^0 + u_z^0)$ and point B$_i$ displaces to $(x + u_x, y + u_y, z + u_z)$. Displacement vector u of a point on a body, is a function of position:

$$u = u(x, y, z) \tag{4.3}$$

Since $A_i B_i$ is infinitesimal we may expand $u(x, y, z)$ around point A$_i$:

$$u = u(x^0, y^0, z^0) + \frac{\partial u_x}{\partial x}(x - x^0) + \frac{\partial u_y}{\partial x}(x - x^0) + \frac{\partial u_z}{\partial x}(x - x^0) + \frac{\partial u_x}{\partial y}(y - y^0) \cdots \tag{4.4}$$

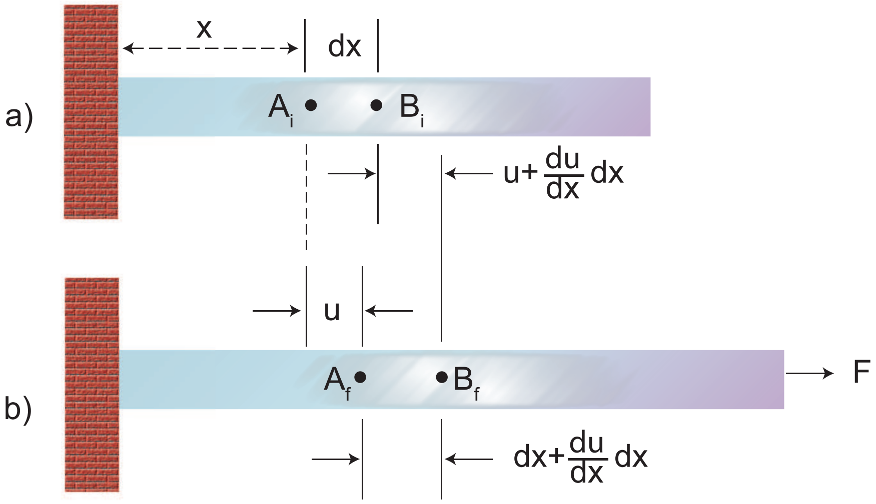

Figure 4.1: Deformation of a bar in one dimension as a result of force F applied to one end and the other end kept fixed. Figure adopted from Fig. 2.1 of Ref. [47].

We may write Eq.4.4 in a compact form using Einstein's summation convention:

$$u_i = u_i^0 + \frac{\partial u_i}{\partial x_j} dx_j. \tag{4.5}$$

In Eq. 4.5 u_i is the i^{th} component of displacement vector and second term stands for a summation over index j. Second term of Eq. 4.5 nothing but gradient of a vector which is a second-order tensor. Second term of Eq. 4.5 is called *deformation gradient* and can be written as a sum of its symmetric and anti-symmetric parts.

$$u_i = u_i^0 + \frac{1}{2}\left(\frac{\partial u_i}{\partial x_j} + \frac{\partial u_j}{\partial x_i}\right) dx_j + \frac{1}{2}\left(\frac{\partial u_i}{\partial x_j} - \frac{\partial u_j}{\partial x_i}\right) dx_j \tag{4.6}$$

The symmetric part of deformation gradient is *strain tensor* (ϵ_{ij})[47]:

$$\epsilon_{ij} = \frac{1}{2}\left(\frac{\partial u_i}{\partial x_j} + \frac{\partial u_j}{\partial x_i}\right).; \tag{4.7}$$

And the anti-symmetric part of deformation gradient is *rotation tensor* (ω_{ij}) [47]:

$$\omega_{ij} = \frac{1}{2}\left(\frac{\partial u_i}{\partial x_j} - \frac{\partial u_j}{\partial x_i}\right). \tag{4.8}$$

Another measure of strain is called Lagrangian strain which is similar to derived above:

$$E = \frac{1}{2}(D^T D - I) \tag{4.9}$$

where D is the deformation gradient tensor with components:

$$D_{ij} = \frac{\partial u_i}{\partial x_j}, \tag{4.10}$$

and I is identity matrix [48].

4.2.2 Discrete Strain Formulation

In the language of geometry, strain is defined through an affine transformation that maps the undeformed state to deformed state, which is called deformation gradient. Several methods to derive discrete form of deformation gradient from atomic positions are reported [48–50]. In this subsection we will present discrete strain formulation proposed by Gullett *et al.*[48] and we will mention another one proposed by Pryor *et al* [49].

The absence of a continuous deformation field prevents usage of continuum strain formalism to derive strain tensor from atomistic simulation data [48]. In Fig. 4.2 we present an atomic system deformed by a deformation gradient **G**. The position of ith atom moved from $\mathbf{x_i^0}$ to $\mathbf{x_i}$. Local deformation gradient tensor is characterized by changes in relative positions of atoms. The position of ith atom's neighbor jth atom moved from $\mathbf{x_j^0}$ to $\mathbf{x_j}$. As a result of deformation, distance between atom i and atom j is changed from $\mathbf{x_{ij}^0}$ to $\mathbf{x_{ij}}$. There exist a unique linear affine transformation that connects, relative positions of atom i and atom j before and after the deformation [48]:

$$\mathbf{x_{ij}} = G^i \mathbf{x_{ij}^0}. \tag{4.11}$$

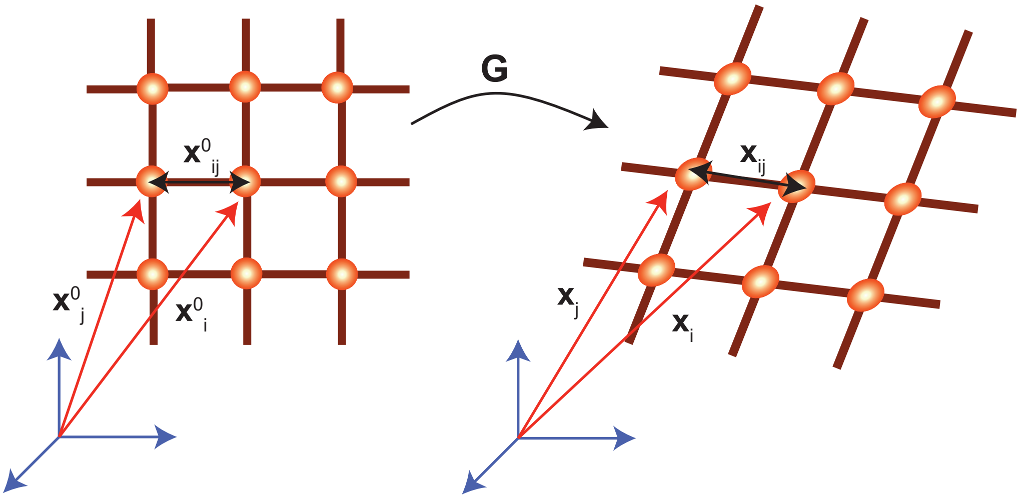

Figure 4.2: Deformation of a discrete atomic system as a result of deformation gradient **G** .

Transformation matrix G^i which maps $\mathbf{x^0_{ij}}$ to $\mathbf{x_{ij}}$ is deformation gradient at atom i. Writing Eq. 4.11 for other neighbors of ith atom, leads to a set of linear equations. Usually for different neighbors of ith atom will result different transformation matrices. We should find an optimal transformation matrix $\hat{G}^i$, which maps all of the neighbors of ith atom with a minimum error. The mapping error of the transformation of ith atom's neighbor jth atom is [48]:

$$\phi^{ij} = (\mathbf{x_{ij}} - \hat{G}^i \mathbf{x^0_{ij}})^T (\mathbf{x_{ij}} - \hat{G}^i \mathbf{x^0_{ij}}) \tag{4.12}$$

If we sum these errors for all neighbors of ith with a proper weights ω_j for every neighbor of ith atom, we will find total mapping error on this atom:

$$\phi^i = \sum_{j=1}^{N} (x_{ij} - \hat{G}^i x^0_{ij})^T (x_{ij} - \hat{G}^i x^0_{ij}) \omega_j \tag{4.13}$$

where N is the number of neighbors of ith atom and w_j is the weighting factor. The optimal transformation matrix $\hat{G}^i$ can be found by minimizing Eq. 4.13 with respect to $\hat{G}^i$: [48]

$$\frac{\partial \phi^j}{\partial \hat{G}^i_{kl}} = \sum_{j=1}^{N} (-2x_{ij,k}x^0_{ij,l} + 2x^0_{ij,l}\hat{G}^i_{kl}x^0_{ij,k})\omega_n = 0 \tag{4.14}$$

where $x_{ij,k}$ is the kth component of vector $\mathbf{x_{ij}}$. Solving Eq. 4.14 for components of $\hat{G}^i$ will leads to:

$$\hat{G}^i_{kl} \sum_{j=1}^{N} x^0_{ij,l}x^0_{ij,k}\omega_j = \sum_{j=1}^{N} x_{ij,k}x^0_{ij,l}\omega_j. \tag{4.15}$$

In matrix notation:

$$\hat{G}^i \sum_{j=1}^{N} \mathbf{x^0_{ij}}\mathbf{x^0_{ij}}^T \omega_j = \sum_{j=1}^{N} \mathbf{x_{ij}}\mathbf{x^0_{ij}}^T \omega_j, \tag{4.16}$$

or

$$\hat{G}^i \mathbf{D} = \mathbf{A}. \tag{4.17}$$

Here **D** and **A** are matrices :

$$\mathbf{D} = \sum_{j=1}^{N} \mathbf{x^0_{ij}}\mathbf{x^0_{ij}}^T \omega_j, \tag{4.18}$$

and

$$\mathbf{A} = \sum_{j=1}^{N} \mathbf{x_{ij}}\mathbf{x^0_{ij}}^T \omega_j. \tag{4.19}$$

We can calculate matrices **A** and **D** from positions of atoms. To find the optimal local deformation matrix $\hat{G}^i$ at ith atom, we can multiply Eq. 4.18 with inverse of **D** from right [48]:

$$\hat{G}^i = \mathbf{A}\mathbf{D}^{-1}. \tag{4.20}$$

Another method, similar to the aforementioned one, to derive local deformation gradient is proposed by Pryor *et al* [49]. In this method, the atomistic strain tensor is derived from local transformation matrix that transforms nearest neighbors of a certain atom from its undeformed state to the deformed one.

Consider the tetrahedron formed by atom i with its four neighbors shown in Fig. 4.3. Distance vector between two neighbors of atom i is changed from $\mathbf{R}^0_{mn}$ to $\mathbf{R}_{mn}$ as a result of local deformation tensor G^i.

$$\mathbf{R}_{mn} = G^i \mathbf{R}^0_{mn}. \tag{4.21}$$

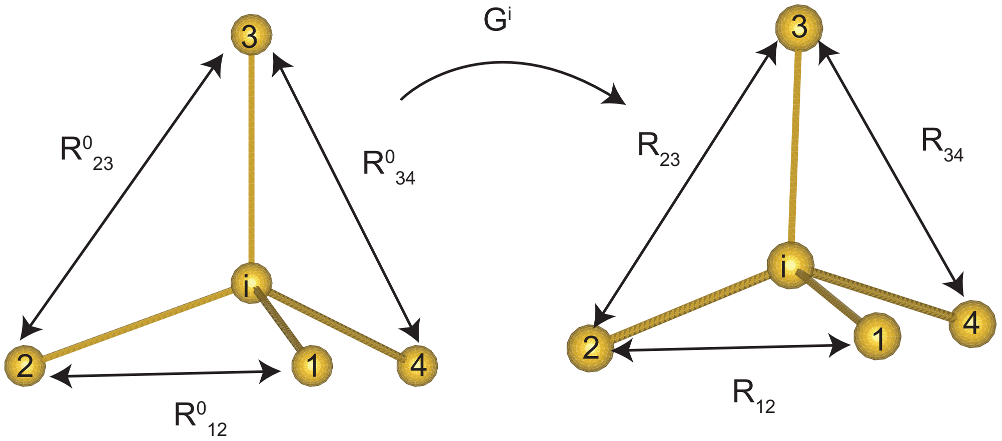

Figure 4.3: Deformation of a tetrahedron as a result of deformation gradient **G**.

Writing relation in Eq. 4.21 for $\mathbf{R}^0_{12}$, $\mathbf{R}^0_{23}$, $\mathbf{R}^0_{34}$ in a compact form [49]:

$$\begin{pmatrix} R_{12,x} & R_{23,x} & R_{34,x} \\ R_{12,y} & R_{23,y} & R_{34,y} \\ R_{12,z} & R_{23,z} & R_{34,x} \end{pmatrix} = \begin{pmatrix} G^i_{xx} & G^i_{yx} & G^i_{zx} \\ G^i_{xy} & G^i_{yy} & G^i_{zy} \\ G^i_{xz} & G^i_{yz} & G^i_{zz} \end{pmatrix} \times \begin{pmatrix} R^0_{12,x} & R^0_{23,x} & R^0_{34,x} \\ R^0_{12,y} & R^0_{23,y} & R^0_{34,y} \\ R^0_{12,z} & R^0_{23,z} & R^0_{34,x} \end{pmatrix} \tag{4.22}$$

Pryor *et al.* proposed a similar strain tensor:

$$\epsilon^{\mathbf{i}} = \mathbf{G}^{\mathbf{i}} - \mathbf{I}, \tag{4.23}$$

where I is the 3x3 identity tensor. We can derive the local strain tensor $\epsilon^{\mathbf{i}}$ at atom i by calculating the inverse of the matrix formed by distance vectors of atom i before deformation:

$$\begin{pmatrix} \epsilon^i_{xx} & \epsilon^i_{yx} & \epsilon^i_{zx} \\ \epsilon^i_{xy} & \epsilon^i_{yy} & \epsilon^i_{zy} \\ \epsilon^i_{xz} & \epsilon^i_{yz} & \epsilon^i_{zz} \end{pmatrix} = \begin{pmatrix} R_{12,x} & R_{23,x} & R_{34,x} \\ R_{12,y} & R_{23,y} & R_{34,y} \\ R_{12,z} & R_{23,z} & R_{34,x} \end{pmatrix} \times \begin{pmatrix} R^0_{12,x} & R^0_{23,x} & R^0_{34,x} \\ R^0_{12,y} & R^0_{23,y} & R^0_{34,y} \\ R^0_{12,z} & R^0_{23,z} & R^0_{34,x} \end{pmatrix}^{-1} . \tag{4.24}$$

From results of the MD simulations, using positions of NC atoms, we first extract each atom's displacement vector from its undeformed site. To find the undeformed state from atomic positions of deformed state, we consider a tetrahedron formed by an atom i and its four nearest neighbors. The idea is to position an ideal tetrahedron formed in bulk case with a minimum error. We first consider bonds between atom i and its neighbors. We choose among them with a length closest to bulk value. We set this bond to ideal tetrahedron's primary axis shown in Fig. 4.2.2-a. Next we consider angles between these bonds and choose another bond among these which makes angle with a value closest to bulk value. We rotate ideal tetrahedron around its primary axis to match other axis to this bond (Fig. 4.2.2-b). With these two steps we position an ideal tetrahedron to deformed local geometry and calculate local strain tensor at atom i via distance vectors between this ideal tetrahedron edges to positions of atom i's neighbors. Using these displacement vectors, we construct deformation matrix and derive the atomistic strain tensor from this local deformation tensor [49].

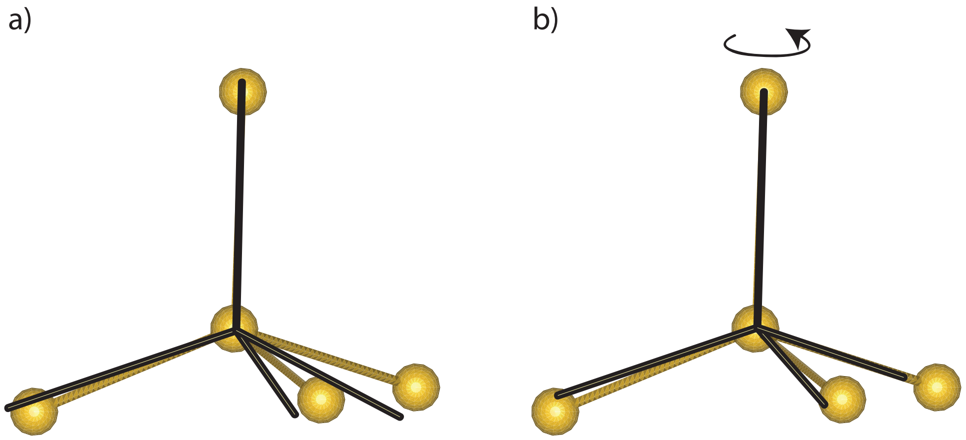

Figure 4.4: Illustration of positioning an ideal tetrahedron to local geometry in two steps.

4.2.3 Hydrostatic and Volumetric Strain

Although strain is a second order tensor it is usually measured with its first invariant, which is called the hydrostatic strain [47]:

$$\epsilon_{hs} = \frac{1}{3}\mathrm{Tr}(\epsilon). \tag{4.25}$$

As an alternative measure to hydrostatic strain, we calculate volumetric strain by considering volume change of a tetrahedron from its undeformed counterpart. Consider the tetrahedron in Fig. 4.3. The edges of this tetrahedron are $\mathbf{R_1^0}$, $\mathbf{R_2^0}$, $\mathbf{R_3^0}$ and $\mathbf{R_4^0}$. The volume of this tetrahedron is:

$$V^0 = \frac{1}{6}\det\begin{vmatrix} R^0_{12,x} & R^0_{23,x} & R^0_{34,x} \\ R^0_{12,y} & R^0_{23,y} & R^0_{34,y} \\ R^0_{12,z} & R^0_{23,z} & R^0_{34,x} \end{vmatrix}. \tag{4.26}$$

Where $R_{12,y}$ is the y component of $\mathbf{R_2} - \mathbf{R_1}$. After deformation the volume of deformed tetrahedron in Fig. 4.3 is:

$$V = \frac{1}{6}\det\begin{vmatrix} R_{12,x} & R_{23,x} & R_{34,x} \\ R_{12,y} & R_{23,y} & R_{34,y} \\ R_{12,z} & R_{23,z} & R_{34,x} \end{vmatrix} \tag{4.27}$$

If we calculate the determinants of both sides of Eq. 4.22:

$$\det\begin{vmatrix} R_{12,x} & R_{23,x} & R_{34,x} \\ R_{12,y} & R_{23,y} & R_{34,y} \\ R_{12,z} & R_{23,z} & R_{34,x} \end{vmatrix} = \det\left|\begin{pmatrix} G^i_{xx} & G^i_{yx} & G^i_{zx} \\ G^i_{xy} & G^i_{yy} & G^i_{zy} \\ G^i_{xz} & G^i_{yz} & G^i_{zz} \end{pmatrix} \times \begin{pmatrix} R^0_{12,x} & R^0_{23,x} & R^0_{34,x} \\ R^0_{12,y} & R^0_{23,y} & R^0_{34,y} \\ R^0_{12,z} & R^0_{23,z} & R^0_{34,x} \end{pmatrix}\right| \tag{4.28}$$

We can rewrite Eq. 4.28 using determinant property:

$$\det \mathbf{R} = \det(\mathbf{G^i})\det(\mathbf{R^0}) \tag{4.29}$$

If we use the strain tensor proposed by Pryor *et al.* and using Eq. 4.26 and Eq. 4.27 we can further rewrite Eq. 4.29:

$$\frac{1}{6}V = \det(\epsilon^{\mathbf{i}} + \mathbf{I})\frac{1}{6}V^0, \tag{4.30}$$

where V^0 and V are volume of tetrahedron before and after deformation respectively. We can write determinant in Eq. 4.30 in terms of multiplication of eigenvalues of:

$$\det(\epsilon^{\mathbf{i}} + \mathbf{I}) = \prod_{j=1}^{3}(\epsilon_j + 1), \tag{4.31}$$

where ϵ_j is jth eigenvalue of strain tensor. For small deformations we can approximate eigenvalues of strain tensor with its average value:

$$\epsilon_1 = \epsilon_2 = \epsilon_3 = \frac{1}{3}\sum_{j}^{3} \epsilon_j. \tag{4.32}$$

Using the fact that sum of eigenvalues of a matrix is equal to its trace, we can write Eq. 4.30 as:

$$\frac{V}{V^0} = (\epsilon_{hs} + 1)^3. \tag{4.33}$$

Finally we can calculate the local hydrostatic strain at an atom by considering volume change of tetrahedron formed by its four neighbors:

$$\epsilon_{hs} = \left(\frac{V}{V^0}\right)^{1/3} - 1. \tag{4.34}$$

We proved that for small deformations, hydrostatic strain can be directly calculated from volumes of tetrahedra. In the next section we also showed that for our system, volumetric strain is similar to the hydrostatic strain.

4.3 Results

We analyze the hydrostatic, volumetric and bond length strain distributions in Si NCs, in particular demonstrate that both compressive volumetric and hydrostatic strain and tensile bond length strain coexist within the same Si NC. We accomplish this by performing trajectory analysis on model samples (with ca. 5000 atoms) simulated via MD using a reliable and accurate as well as reactive force field [16]. The simulation details are similar to those explained in Ch. 3 and Ref. [8]. In this case we construct the Si NC in glass matrix with a slightly different method. Instead of deleting all glass atoms within a predetermined radius, we remove the glass atoms after rigorously defining the surface of the nanocrystal through the Delaunay triangulation method [31]. Delaunay triangulation method is computational geometry tool that defines a closed surface from a set of points in three dimensions. This method has usages

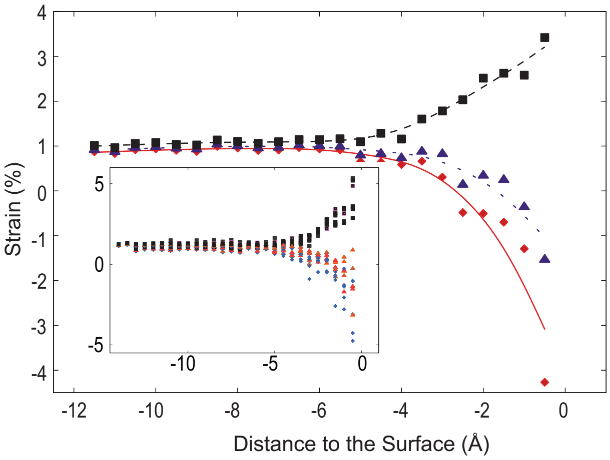

Figure 4.5: Variation of, Si-Si bond lengths (squares), hydrostatic strain (diamonds), and the volumetric strain (triangles) as a function of distance to nanocrystal surface (see text). Dashed, dotted and solid lines are guides to the eye for the respective data set. The data for 2.6 nm diameter NC is used. Inset: Other NC diameters ranging from 2.2 nm to 3.2 nm are also shown.

in different areas but we are the first to use this tool to define a nanocrystal surface. In this way, we have constructed NCs embedded in glass matrix with diameters ranging from 2.2 nm to 3.2 nm without introducing built-in strain to the system. In this diameter range we observe similar trends in strain, volumetric strain, and bond length distribution etc., therefore, we present only the figures of the system for a typical NC of radius 2.6 nm.

To verify our results we have calculated strain distribution in NC region for all mentioned measures. We have plotted all three of them in Fig. 4.5. The results of volumetric strain are very close to hydrostatic strain which is the trace of strain tensor calculated with aforementioned technique [49]. In previous section we already showed these two are similar in the limit of small deformations. In these results, we observe a net compressive behavior of strain just under the surface and a uniform tensile strain of about 1% at the core of NC. Si-Si bonds are stretched by about 1% in the core region in agreement with the hydrostatic and volumetric strains, however, just under the surface, Si-Si bonds are stretched

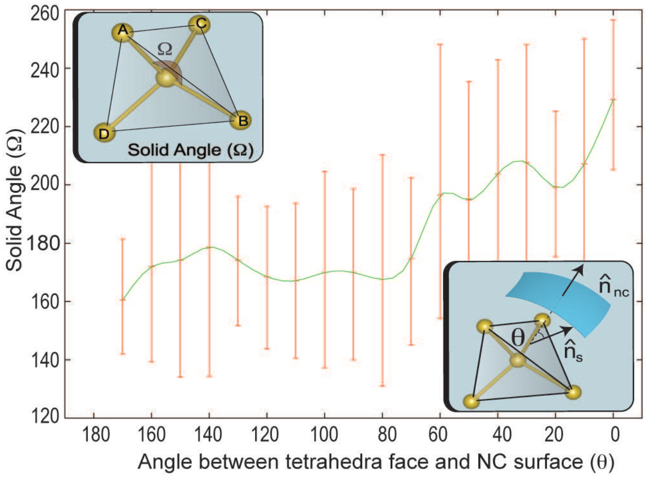

Figure 4.6: Dependence of solid angle subtended by tetrahedron face to the angle between tetrahedron face and nanocrystal surface. Illustration of solid angle subtended by tetrahedron face (top left inset) and the angle between tetrahedron face and NC surface (bottom right inset).

up to 3% where hydrostatic and volumetric strain results indicate compressive strain state. The bond-stretch in Si-Si bonds due to oxidation has been shown earlier by us using molecular dynamics simulations [8] which was also confirmed by other approaches [46].

Occurrence of compressive volumetric strain and stretched bond lengths in the same outer region may initially seem contradicting. However, stretching of bonds does not imply that the system is under tensile hydrostatic strain as well. Consider a tetrahedron formed by a Si atom and its four Si neighbors (A, B, C, D) as shown in upper inset of Fig. 4.6. In the ideal case, the solid angle (Ω) subtended by each triangular face of this tetrahedron should be equal to 180°. Under a uniform deformation, bond lengths will also be stretched, while the solid angles remain unchanged. However, under a nonuniform deformation, the change in three solid angles causes a decrease in the volume of the tetrahedron while increasing or preserving the bond lengths. Hence, a combination of stretched bond lengths with deformed solid angles may end up with an overall reduction of the volume of the tetrahedron. This explains the coexistence of compressive volumetric strain and stretched bond lengths at the region just below the surface of NCs.

To better visualize the nature of the deformation of the Si NCs, we consider the orientational variation of the solid angles of the tetrahedral planes. As illustrated in the lower inset of Fig. 4.6, the two important directions are the unit normal ($\hat{n}_{\mathrm{S}}$) of the tetrahedron face subtending the solid angle under consideration, and the local outward surface normal ($\hat{n}_{\mathrm{NC}}$) of the NC. It is clearly seen from Fig. 4.6 that solid angles subtended by tetrahedra faces oriented outward to the NC surface are increased up to 220°, whereas those facing inward to the NC core are decreased down to 160°. This dependence is a clear evidence of how oxidation affects strain distribution close to the interface.

To further quantify the atomistic strain in the highly critical region within 3 Å distance to the interface, we classify the average bond length and hydrostatic strain behaviors into three categories. Fig. 4.7 displays the percentage as well as the bonding details of each category. In top-left, we illustrate most common type with a share of 53.0% which is responsible for the opposite behavior in Fig. 4.5 where average bond lengths of center Si atoms to its four nearest neighbors are stretched but net atomistic strain at this atom is compressive. In this case solid angles facing toward the oxide region is increased to 270° due to oxygen bonds of Si neighbors. Although these oxygen bonds stretched Si-Si bonds to 2.41 Å, net strain on center Si atom is -2.7%. In the top-right part of the Fig. 4.7 we illustrate second most often case with a percentage of 42.0%, where average bond lengths and atomistic strain show similar behavior; bond lengths are stretched and net hydrostatic strain is tensile. In this case oxidation somewhat uniformly deforms the bonds so that solid angles are still around 180° which is the value for the unstrained case. Finally, as shown at bottom of Fig. 4.7, a very small percentage of atoms (5.0%) in the region beneath the surface have shortened bond lengths and compressive atomistic strain.

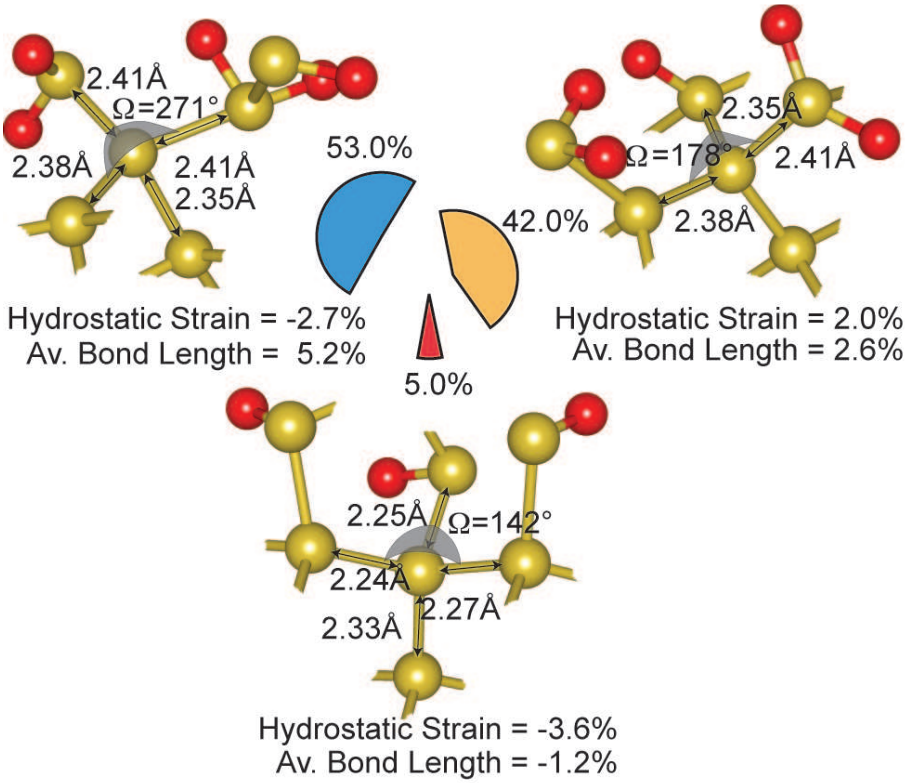

Figure 4.7: Illustrations of oxidation effects on strain in three categories with their percentage of occurrences: Si-Si bonds are stretched and system is under compressive strain (upper left). Si-Si bonds are stretched and system is under tensile strain (upper right). Si-Si bonds are shortened and the Si atom at the center is under compressive strain (bottom). Large spheres (gold) and small spheres (red) represents Si and O atoms, respectively.

You don't wonder where we're going
Or remember where we've been
We've got to keep this traffic
Flowing and accept a little spin
Cake, "The Long Line of Cars",
Comfort Eagle, Columbia Rec. 2001.

I see a red door and I want it painted black
No colors anymore I want them to turn black
Rolling Stones, "Paint It Black",
Aftermath, ABKCO Records. 1966.

Chapter 5

Vibrational Spectra of Embedded Si Nanocrystals

5.1 Introduction

Velocity autocorrelation function (VACF) is one of the most used member of the time dependent correlation functions family. Various dynamical properties of a system can be calculated using VACF such as diffusion coefficient, thermal conductivity etc. We used VACF to obtain vibrational density of states of the system. In this part of the Thesis we present technical details of VACF by considering silicon and silica as case studies.

5.2 Velocity Autocorrelation Function

Time dependent correlation functions are measures of correlations of various quantities at different times. Suppose that we are carrying out Molecular Dynamics (MD) simulations and we have N atoms in our system. At a finite temperature every atom in the system has a kinetic energy and vibrating around its equilibrium position with some frequency. Correlation of these atoms' velocities at different times depends on their vibration frequencies. We record velocities of atoms at desired time intervals and to extract these frequencies we first construct VACF at every time step:

$$c(t) = \frac{1}{N}\sum_{i=1}^{N} v_i(t)\cdot v_i(t_0). \tag{5.1}$$

In 5.1 N is the number of atoms in the system. For next time step of simulation:

$$c(t+\Delta t) = \frac{1}{N}\sum_{i=1}^{N} v_i(t+\Delta t)\cdot v_i(t_0). \tag{5.2}$$

Normalizing VACF by dividing it with its value at t_0:

$$C(t) = \frac{c(t)}{c(t_0)} \tag{5.3}$$

gives us a time series resembling VACF starting with a value 1 at $t = t_0$

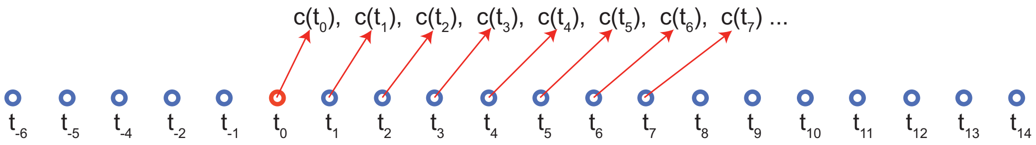

Figure 5.1: Construction of correlation function starting from a chosen time origin t_0.

converging to 0 with time (Fig. 5.1). In Fig. 5.2 we present VACF for bulk silicon system with 216 atoms. Periodic boundary conditions applied for all directions. As time goes on, relation of velocities decreases and VACF converges to zero. We can continue to calculate VACF as much as we can do, but we are always limited with computational power and storage resources so we stop simulation after having enough number of data from the simulation. If the system is in thermal equilibrium then VACF is independent of starting time (t_0), so we start constructing VACF after waiting the system to reach its thermal equilibrium. Since VACF is independent from time origin (t_0) we may construct different VACF's by choosing different time origins (Fig. 5.3). Instead of constructing a single, long time series of VACF, we construct multiple VACFs by selecting

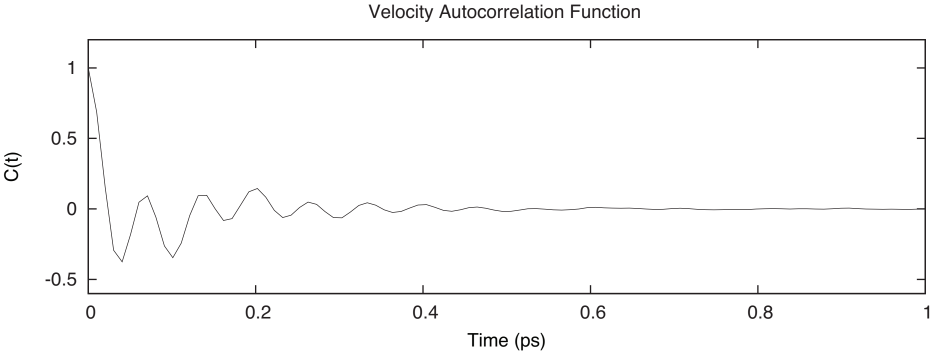

Figure 5.2: Velocity autocorrelation function for bulk silicon system consisting 216 atoms.

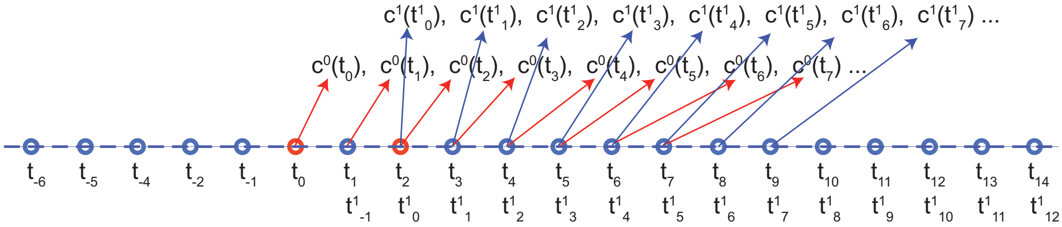

Figure 5.3: Construction of correlation function starting from different time origins.

different time origins and we add these VACFs ($c^i(t)$) to have an average VACF:

$$C_{av}(t) = \frac{1}{N_v}\sum_{j=1}^{N_v} c^j(t). \tag{5.4}$$

In Eq. 5.4, N_v is the number of VACFs constructed by choosing N_v different time origins. Suppose that we run a MD simulation and we record velocities of atoms for N consequent time steps. Lets say that at $t = t_s$ system has reached its thermal equilibrium. If we construct VACFs by choosing equally spaced time origins, say Δt_v, and starting from $t = t_s$ we have $n = N - t_s - N_v\Delta t_v$ time steps for every VACF. Larger time series for VACF gives better resolution in vibrational frequencies but calculating multiple VACFs will give accurate results free from statistical errors. Since we have a definite number of time series recorded during simulations, increasing number of time steps for every VACF will decrease the number of VACFs vice versa. Now the question arises: How can we determine the number of time steps for every VACF? If we consider Fig. 5.2 we observe that VACF will converge to zero after 0.6 ps. Constructing VACF that spans much more time than 0.6 ps would be unnecessary for this case. Another criterion to determine the number of time steps between two VACFs is average period of the oscillations of the system. If time step between two VACFs is shorter than this period this means that we are sampling same oscillations more than once and this would be an unnecessary computation.

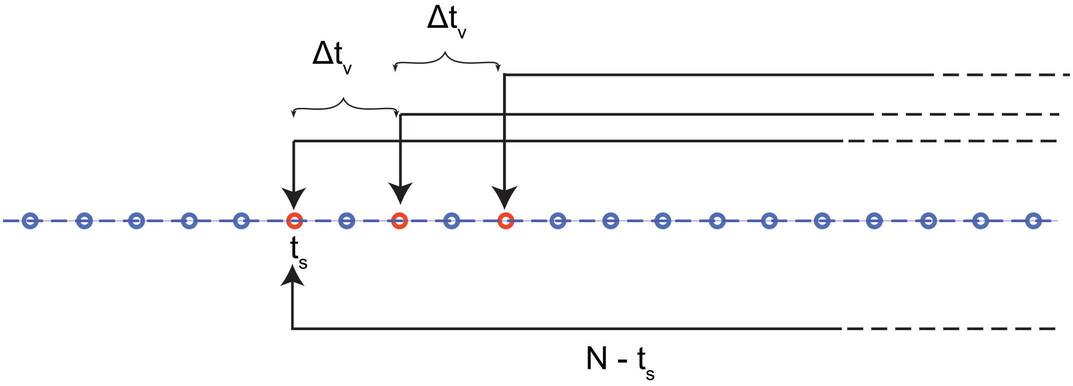

Figure 5.4: Number of time steps for every VACF.

Although we can calculate various thermodynamical properties of system we are interested in vibrational frequencies of atoms around their equilibrium positions. All of atoms in the system contribute to VACF with their vibrational frequencies so VACF is just like a sum of signals with various frequencies. To extract how many atoms are vibrating at each frequency or in other words density of vibrational states, we calculate the Fourier transform of VACF. In the next section of this chapter we focus on details of Fourier transform of discretely sampled data.

5.3 Fourier Transform of Discretely Sampled Data

Any function whether it is periodic or not can be written in terms of linear combination of sines or cosines:

$$g(t) = \sum_{i=1}^{\infty} h_i \cos(2\pi f_i t). \tag{5.5}$$

If we write in integral form of Eq 5.5:

$$g(t) = \int_{-\infty}^{\infty} h(f) \cos(2\pi f t) df. \tag{5.6}$$

We may also write in complex form of Eq 5.6:

$$g(t) = \int_{-\infty}^{\infty} h(f) e^{-i2\pi f t} df. \tag{5.7}$$

Eq 5.7 states that a function $g(t)$ in time domain can be represented by sum (integral) of other functions $h(f)$'s in frequency domain. This means that the operation in Eq 5.7 transforms $h(f)$ to $g(t)$ from frequency domain to time domain. This operation called inverse Fourier transform and similarly the operation which transforms $g(t)$ in time domain to $h(f)$ in frequency domain called Fourier Transform [15]:

$$h(f) = \int_{-\infty}^{\infty} g(t) e^{i2\pi f t} dt. \tag{5.8}$$

Like our situation, usually the function $g(t)$ is recorded (sampled) at N equally spaced time intervals:

$$g_n = g(n\Delta t) \qquad n = 0, 1, 2, 3...N \tag{5.9}$$

Sampling rate which is the amount of data recorded per second defines the *Nyquist Frequency*, half of the sampling rate:

$$f_c = \frac{1}{2\Delta t}. \tag{5.10}$$

The importance of *Nyquist Frequency* revealed by sampling theorem which states that: *Fourier Transform of a continuous function $g(t)$ sampled with equally spaced time intervals (Δt) is bandwidth limited to frequencies smaller than f_c* [15]. Since we have discrete values of function $g(n\Delta t)$ in time domain, to transform $g(t)$ into frequency domain $h(f)$, we need to approximate the integral in Eq 5.8 by a discrete sum [15]:

$$h(f_k) = \frac{1}{2\pi}\int_{-\infty}^{\infty} g(t)e^{i2\pi f_k t}dt = \frac{1}{2\pi}\sum_{n=0}^{N-1} g_n e^{2\pi f_k t_n}\Delta t = \Delta t \sum_{n=0}^{N-1} g_n e^{2\pi nk/N} \tag{5.11}$$

where $f_k = \frac{n}{N} f_c$. If we write :

$$h(f) = h_k \frac{\Delta t}{2\pi}. \tag{5.12}$$

This procedure transforms N complex numbers g_n's into h_k's and is called Discrete Fourier Transform [15]:

$$h_k = \sum_{n=0}^{N-1} g_n e^{2\pi kn/N}. \tag{5.13}$$

5.4 Vibrational Density of States of Crystalline Silicon

With this insight we transform VACF from time domain to frequency domain. Hence we have density of each frequency in the vibrational spectrum which is called Vibrational Density of States (VDOS). Before calculating VDOS of bulk silicon, examining the available phonon dispersion curves may give valuable information. In Fig. 5.5 we present phonon dispersion curves calculated with a technique similar to ours [51]. If we look at Fig. 5.5 we should expect a sharp peak at ≈ 15.3 THz, (≈ 510 cm^{-1}) which is transverse optical (TO) vibrational mode of silicon. In literature TO peak of silicon is reported around 520 cm^{-1} (15.6 THz) [52]. Inverse centimeters (cm^{-1}) is the more common unit in this field and 1 THz is equal to 33.35 cm^{-1}. We will use inverse centimeters in this Thesis as the main unit to describe frequency. TO peak of Si at ≈ 520 cm^{-1} is Si-Si bond stretching mode which is the most dense mode in the spectra. Behavior of this mode under strain or at different temperatures are our main interests. We run a MD simulation of bulk silicon consisting of 64 atoms (2x2x2 unit cells). Temperature was set to 200 K and our MD time step was 0.25 fs. We record velocities of atoms for every 50 MD steps. This results in a 12.5 fs time interval Δt. We wait for 50000 MD steps for the system to reach its thermal equilibrium. Then we calculate average VACF over 5000 VACFs by choosing multiple time origins (Δt_v). We calculate VDOS by taking Fourier transform of average VACF. Nyquist frequency of our FT is equal to 1340 cm^{-1}, (40 THz), so our transform is *bandwidth limited* to 1340 cm^{-1}. Since we are interested in frequencies less than 600 cm^{-1} our sampling rate is good enough for our purposes. In Fig. 5.6 we present the graph of this calculation. To further stress the importance of choosing

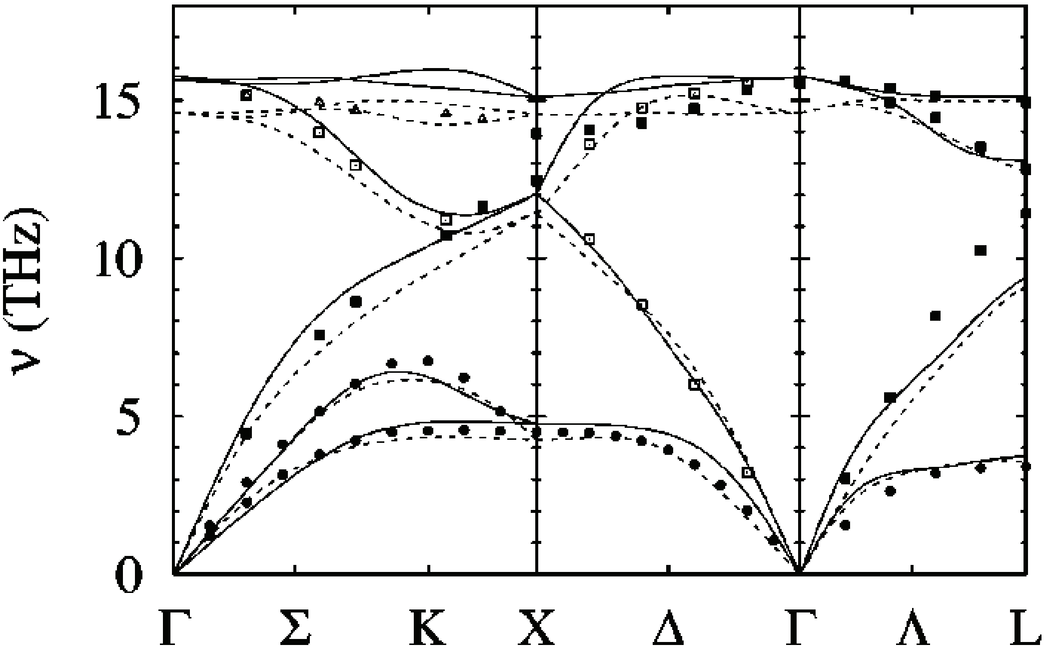

Figure 5.5: Phonon spectra of bulk silicon at different temperatures, solid lines: T=100 K, dashed lines: T=1500 K (Ref [51])

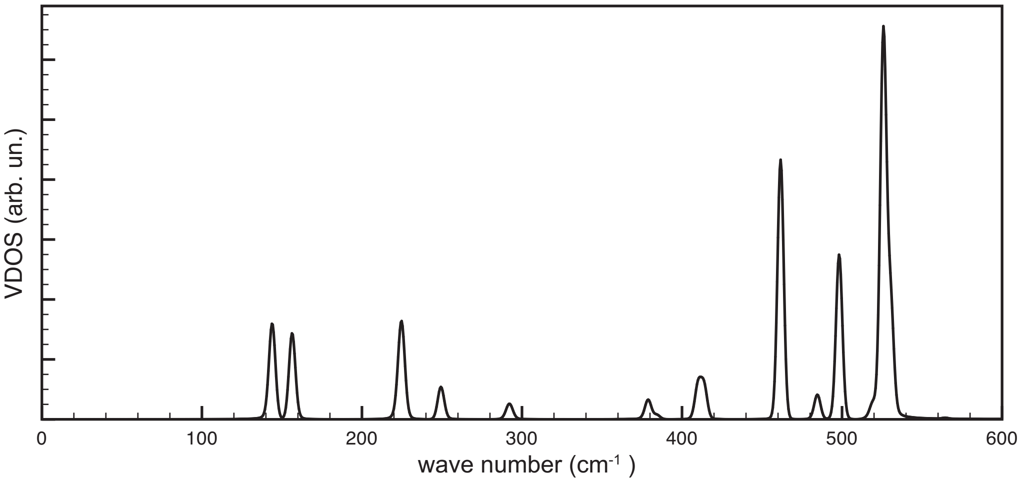

Figure 5.6: VDOS of silicon. Extracted from Fourier transform of VACF averaged from 5000 VACFs constructed by choosing 5000 equally separated time origins. The system consists of 64 atom system at 200 K

.

multiple time origins during the construction of VACF, we also present graph of VDOS of silicon extracted from Fourier transform of VACF constructed from a single time origin instead of 5000 time origins (Fig. 5.7). If we compare dashed line and solid line in Fig. 5.7 we see that averaging from more VACFs results in a smoother curve in VDOS.

We observe TO peak of silicon in Fig. 5.6 at about 525 cm^{-1} which is close to result of Ref. [52]. This peak is a result of Si-Si vibrations. To find out how strain affects VDOS of silicon we apply hydrostatic compressive and tensile strain by rescaling the simulation box uniformly. We apply 2 % and 4 % tensile (compressive) strain by uniformly expanding (compressing) the system. In Fig. 5.8 we observe that under compressive strain TO peak of silicon shifts to higher wave numbers (up to 531 cm^{-1} under 4 % compressive strain) and similarly under tensile strain same peak shifts to lower wave numbers (up to 515 cm^{-1} under 4 % tensile strain). It is easy to understand why TO peaks behave in

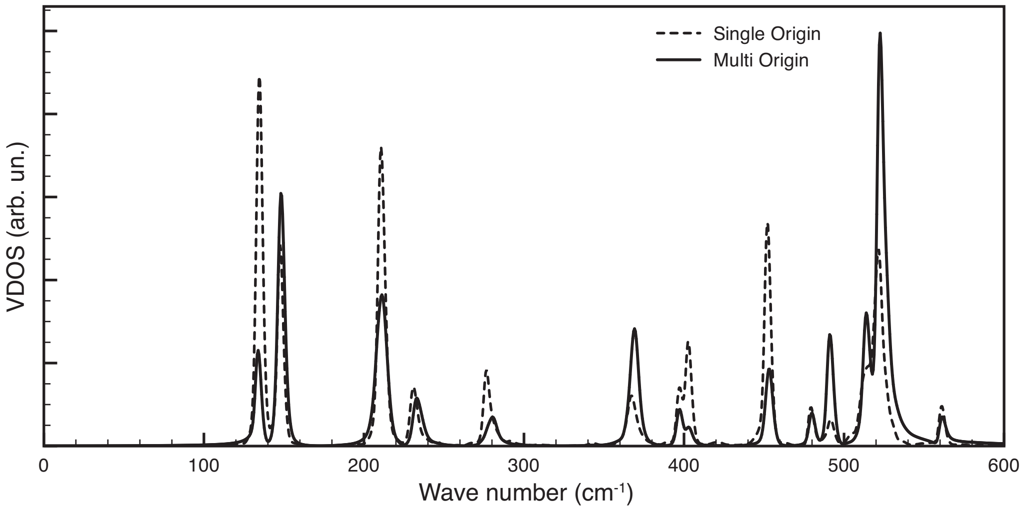

Figure 5.7: VDOS of silicon. Extracted from Fourier transform of VACF averaged from 5000 VACFs constructed by choosing 5000 equally separated time origins (solid line). Extracted from Fourier transform of VACF constructed by choosing single time origin (dashed line). Choosing multi time origins smoothen the data and yields better result. The system consists of 64 atoms at 800 K.

this way under strain if we consider a classical Lennard-Jones potential which is a rough estimate of interaction between two bonded atomsx‘. In Fig. 5.9 we observe that when two atoms become closer than their equilibrium, potential curve gets steeper, this corresponds the compressive strain. Steeper potential means larger force, hence larger force constant so frequency of Si-Si bond stretching mode should increase if we apply compressive strain. On the other hand, when two atoms get apart from each other, potential curve becomes softer hence lower force constant, so the frequency of Si-Si bond stretching mode should decrease if we apply tensile strain. On the contrary, TA peak (162 cm^{-1}) behaves opposite to TO peaks. Under compressive strain TA peak shifts to lower frequencies (up to 136 cm^{-1} under 4 % compressive strain). For the case of tensile strain TA peak shifts to higher frequencies (up to 185 cm^{-1} under 4 % tensile strain) (Fig. 5.10). Increasing temperature has a similar effect like applying tensile strain; when we

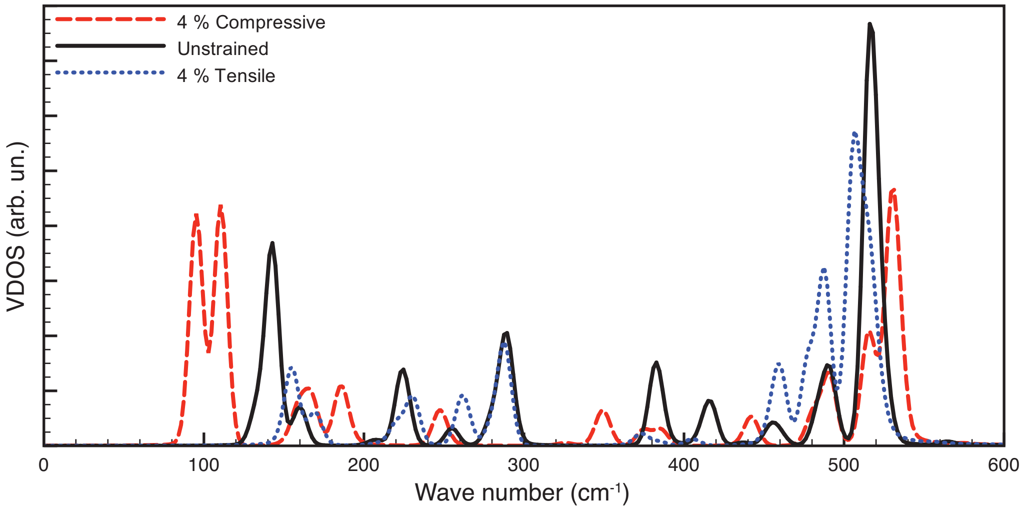

Figure 5.8: Effect of strain to VDOS. Extracted from Fourier Transform of VACF of 64 atom system with hydrostatic strains, at 200 K

.

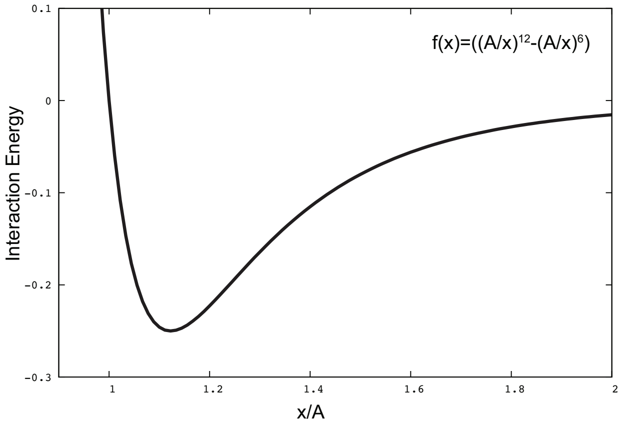

Figure 5.9: Classical Lennard-Jones potential.

.

increase temperature from 100 K to 1500 K TO peak shifted to lower frequencies from 507 cm^{-1} to 492 cm^{-1}. In Fig. 5.11 we present VDOS of crystalline silicon at various temperatures ranging from 100 K to 1500 K. Increasing temperature also broadens the TO peak. Full width at half maximum (FWHM) of TO peaks increases from 87 cm^{-1} to 87 cm^{-1} when we increase the temperature to 1500 K. In Fig. 5.12 we present the temperature dependence of position and FWHM of TO peak of crystalline silicon.

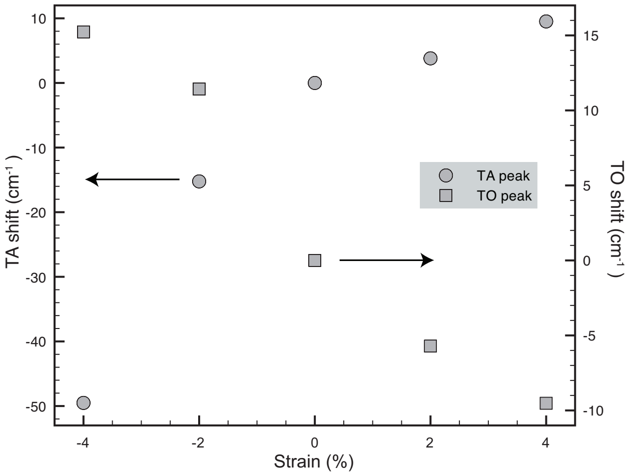

Figure 5.10: Shifts of TO and TA peaks with strain

.

5.5 Vibrational Density of States of Amorphous SiO$_2$

The system that we are dealing with is composed of nanocrystalline silicon embedded in amorphous SiO$_2$ (silica, a-SiO$_2$). To understand the VDOS of this system we should also understand the VDOS of silica. There are several methods to generate an amorphous system. One of the most used method is to mimic simulated annealing process with MD simulation. Starting with a crystalline form of SiO$_2$, increasing the temperature of the system gradually to melting temperature of the system, then cooling the system slowly will yield a

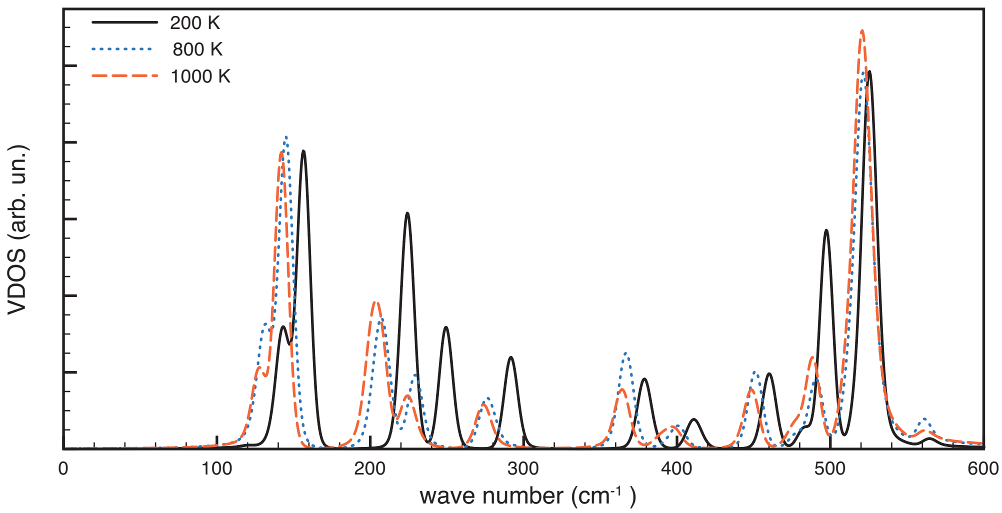

Figure 5.11: Vibrational density of states of crystalline silicon at various temperatures

.

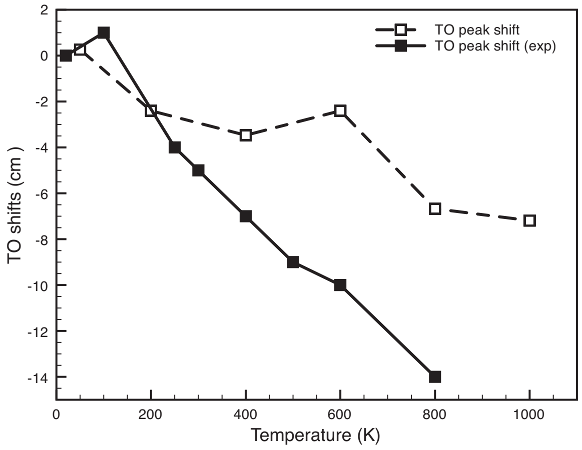

Figure 5.12: Effect of temperature to position of the TO peak of crystalline silicon

.

fine amorphous system. We generate amorphous SiO_2 starting from different crystalline phases of crystalline SiO_2 such as, α-quartz, β-cristobalite, low-cristobalite. We set the density of the system as 2.2 gr/cm^3 by scaling the lattice constants. Our systems consist of about 192 atoms, and simulation box size is about 14.3 Å. In Fig. 5.13 we present the energy of the system during the annealing process. Although different phases start from different energy levels they all end up at the same energy level.

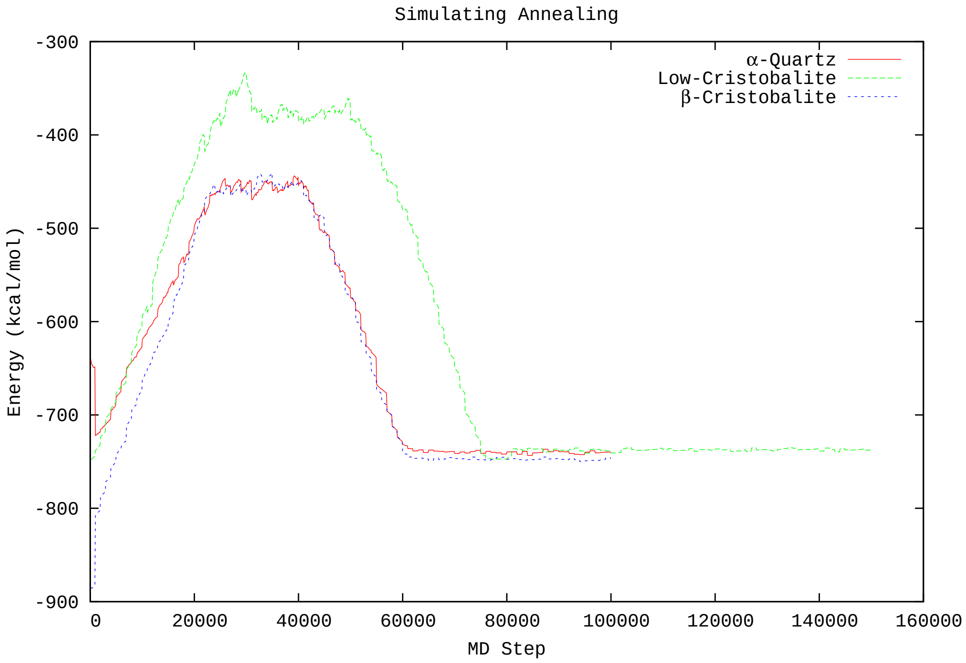

Figure 5.13: Generating amorphous silicon dioxide using MD simulation with simulated annealing

.

After generating amorphous silica using simulated annealing method, we run constant temperature MD simulation to construct VACF of the system. We calculate the Fourier transform of VACF to have VDOS of the system. To compare our results we also present neutron scattering experiment results of Carpenter and Price [53] in Fig. 5.14. There is a fair agreement in trends between our results and experiment. However our technique underestimates phonon frequencies especially those at higher wave numbers. This underestimation originates from the parametrization of the force field. Since we are interested in relative shifts of those peaks, this underestimation does not effect our predictions.

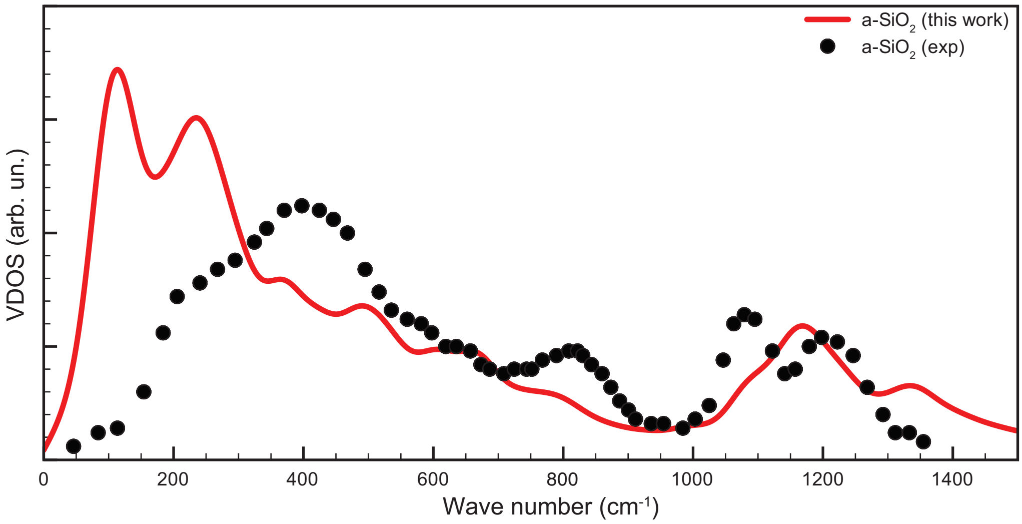

Figure 5.14: Comparison of VDOS of silica systems calculated using ReaxFF (solid line) with neutron scattering experiment results of Ref. [53] (filled circles).

.

When we consider Fig. 5.14 we observe two huge, wide peaks at 113 cm^{-1} and 234 cm^{-1}. These are acoustic vibrations of silica. We have two peaks at around 1164 cm^{-1} and 1330 cm^{-1}. These are asymmetric stretching vibrations of Si-O-Si atoms. There are two TO and two LO modes within 1000 cm^{-1}-1250 cm^{-1} mixed together. The symmetric stretching of Si-O-Si atoms results in a bare peak around 650 cm^{-1}.

Unlike crystalline systems, amorphous structures have no long range order but rather a short range one. In the case of silica, local bonding topology (bond lengths, bond angles etc.) is similar to alpha quartz phase of SiO$_2$ (α-SiO$_2$). Likewise, amorphous structure of silicon also has only the short range order, i.e., silicon atoms form tetrahedra as in the crystalline phase. Vibrational spectra

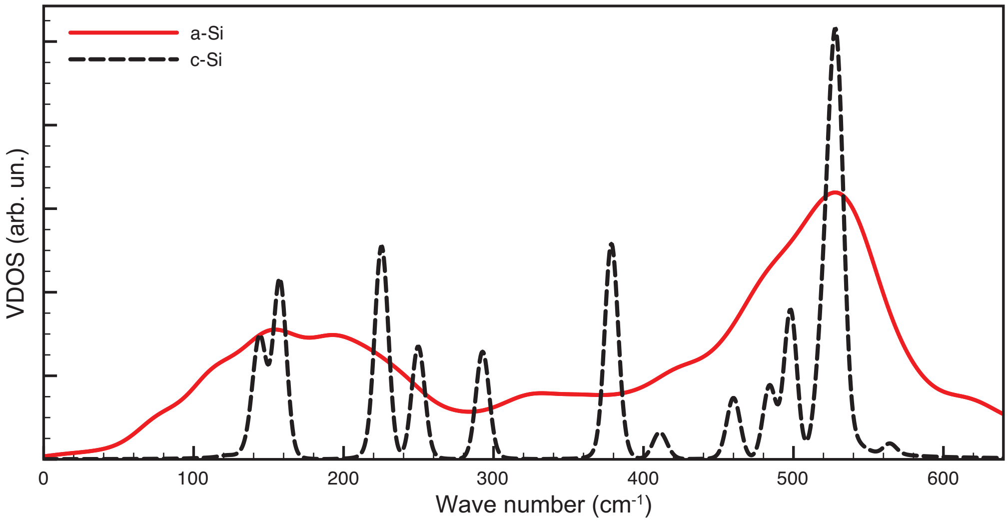

Figure 5.15: Comparison of VDOS of amorphous silicon and crystalline silicon.

.

more or less depends on short range order of a system. We compare the VDOS of amorphous silicon with that of crystalline silicon in Fig. 5.15. We observe in this figure that TO peak of crystalline silicon coincides with the same peak of amorphous silicon which is a direct consequence of the short range order similarity of both structures. It can be observed that the crystalline spectrum has sharp peaks due to the constraints of the crystalline symmetry. In general terms, this figure is a clear demonstration for the broadening of the crystalline spectra as a result of amorphization.

5.6 Painted VACF

5.6.1 Introduction

The eye is one of the magnificent parts of the human body: Photoreceptors in the retina transforms light to electrical signals and send these to brain. Cone type photoreceptors *see* the colors and high sensitive rod type photoreceptors *see* details of the object. The brain processes these signals not only to *see* the objects but also to *perceive* them. Colors of objects affect our perception. In Ch. 5 we presented the calculation of VDOS of a system using MD simulation technique. As case studies we discussed VDOS of silicon related systems, crystalline and amorphous silicon and amorphous silicon dioxide . Those simple systems' atoms are colorless; i.e. they all share the same conditions. On the other hand, Si-NC embedded in amorphous oxide system which we target to understand has several colors needed to be *seen*. In this chapter we introduce our technique called "Painted VACF" which enables us to *perceive* this system better.

5.6.2 Painting Atoms

If we had used the conventional VACF scheme to obtain VDOS of Si-NC embedded in a-SiO_2 system, we would end up with Fig. 5.16. VDOS in Fig. 5.16 contains contributions of *all* atoms of the system. Highly populated acoustic modes mask the contributions of NC atoms at lower wave numbers. We can only identify Si-Si stretching mode at around 515 cm^{-1} from contributions of NC atoms. If we consider our analysis of strain fields in Si-NCs that we present in Ch. 4, all of the NC atoms are not at the same strain state. Contributions of NC atoms with different strain state cannot be addressed with the conventional VACF scheme.

As a remedy, we "*paint*" the atoms in the system with respect to their neighboring atoms. We introduce six color codes as follows:

1. **Core NC atoms:** A silicon atom with all silicon neighbors.
2. **Surface NC atoms:** A silicon atom with at least one Core-NC atom neighbor and at least one oxygen neighbor.
3. **Si-NC bonded Si atoms:** A silicon atom from oxide matrix which is bonded to Si-NC.
4. **Oxide Si:** A silicon atom from oxide matrix which is *not* bonded to Si-NC.

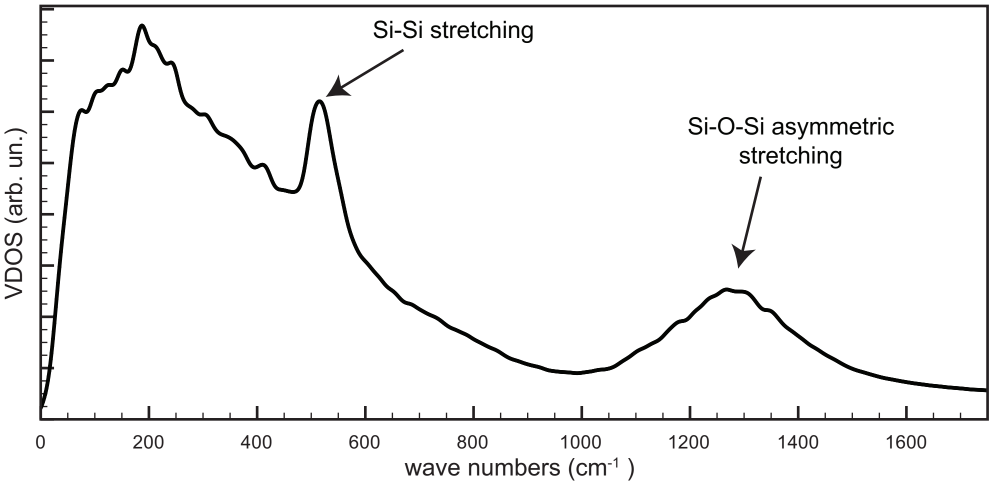

Figure 5.16: VDOS of Si-NC embedded in a-SiO_2 obtained by constructed VACF of all of atoms. The only peaks which contain valuable information are the Si-Si stretching mode at around 515 cm^{-1} and asymmetric stretching mode of Si-O-Si bonds at around 1300 cm^{-1}.

5. **Si-NC bonded O atoms:** An oxygen atom bonded to Si-NC.
6. **Oxide Oxygen:** Oxygen which is **not** bonded to Si-NC.

We record bonding information together with the velocities of atoms during the simulation. We use multi time origin to calculate time average of VACF. Details of VACF construction were described in Ch. 5. Since we use a reactive force field, bond topology of the system evolves during the simulation. Thus updating colors of atoms at every MD step results a change in number of atoms painted with a particular color. This makes VDOS calculation with diffusive modes populated at zero frequency. To prevent this unphysical outcome we paint atom at every time origin only and calculate every VACF by considering colors of atoms at the time origin of that VACF.

5.7 Vibrational Spectra of Embedded Si Nanocrystals

In Ch. 3 we described the procedure of inserting NC into oxide matrix. We use a simulation box of size 3.6 nm. We insert a NC with a diameter of 2.6 nm into this glass system. Before recording velocities we increase the temperature to 600 K and decrease back to room temperature in 30,000 MD steps. After waiting 20,000 steps for the system to reach its thermal equilibrium, we start recording velocities of atoms and bonding topology of the system for every 25 MD step. We continue performing MD simulation for 200,000 MD steps. We set the simulation time step to 0.25 fs. The Nyquist frequency of the constructed VACF is 2668 cm^{-1}.

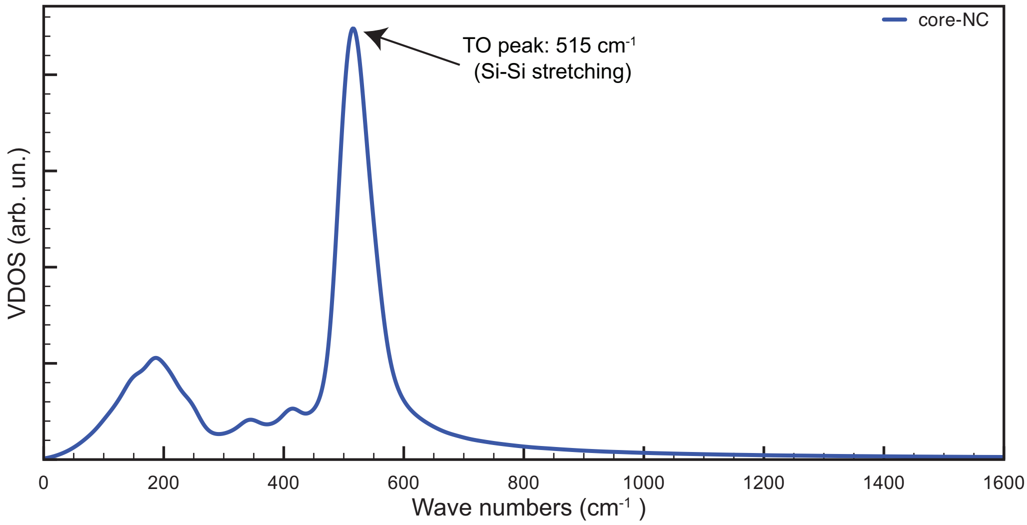

Figure 5.17: VDOS of silicon atoms at the core of NC. TO peak due to Si-Si bond stretching mode can be identified at 515 cm^{-1}.

In Fig. 5.17 we present VDOS of silicon atoms at the core of the NC. The crystalline order is preserved at the core of NC. Thus all the major peaks of vibrational spectra of c-Si are observed in the VDOS of core-NC atoms. The position of TO peak due to Si-Si bond stretching vibrations appear at 515 cm^{-1}.

We compare VDOS of core-NC atoms with the VDOS of silicon atoms at the surface atoms in Fig. 5.18. An interesting observation is that the TO peak of *surface* silicon atoms shift to 494 cm^{-1}. This shift to lower wave numbers with respect to TO peak of core-NC atoms corresponds to stretching of Si-Si bonds of surface-NC atoms due to oxidation. As a matter of fact, in Ch. 4 we showed that oxide matrix that surrounds NC stretches Si-Si bonds just under the NC. Broader peaks of surface Si atoms show the reduction of crystalline order at the surface of NC due to nonuniform deformation [54].

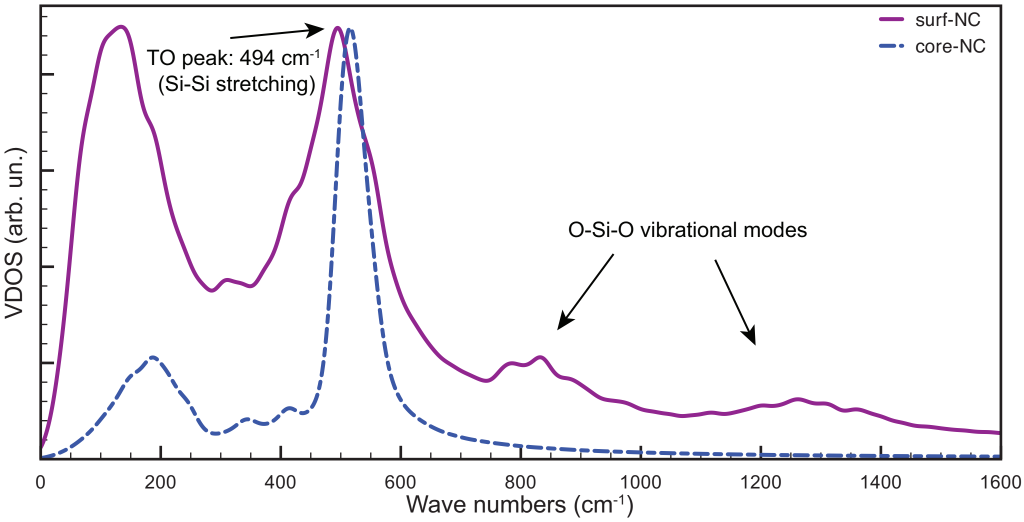

Figure 5.18: VDOS of silicon atoms at the surface of NC (solid line). TO peak due to Si-Si bond stretching mode identified at 494 cm^{-1}. VDOS of core-NC atoms also presented for comparison (dashed line).

Another interesting feature of VDOS of surface Si atoms arises when we compare it with VDOS of silicon atoms in the oxide. O-Si-O system has three vibrational modes. One of them is the symmetric mode at around 800 cm^{-1} and other two are asymmetric vibrational modes at around 1250 cm^{-1}. In Fig. 5.19 we observe that symmetric O-Si-O mode of surface Si atoms shifts to higher wave numbers by about 50 cm^{-1} with respect to same peak of silicon atoms in the oxide. This shift to higher wave numbers resembles stronger Si-O bonds at the

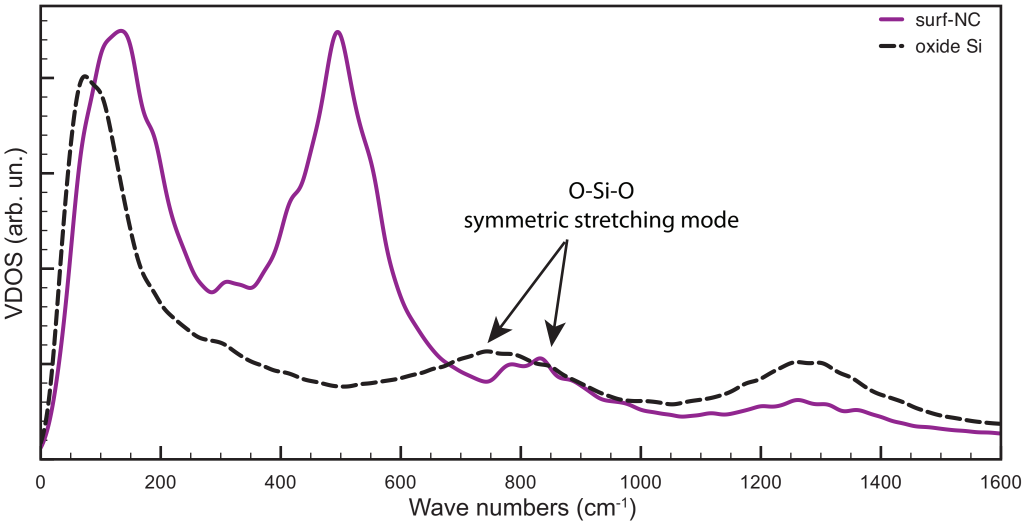

Figure 5.19: VDOS of silicon atoms at the surface of NC (solid line). The symmetric mode of O-Si-O vibrations of surface Si atoms shifts to higher wave numbers with respect to same mode of Si atoms at the oxide. VDOS of oxide Si atoms also presented for comparison (dashed line).

surface of NC with respect to those at the oxide.

5.8 Conclusion

Introducing a novel technique as we called “Painted VACF” enables us to extract valuable information from the vibrational spectra of the system. First of all we observe that core of NC preserves it crystalline order. On the other hand oxidation causes deformation at the surface of the NC. The VDOS of these atoms reveals the degradation in the crystalline order. The TO peak due to Si-Si bond stretching of surface Si atoms shifts to lower wave numbers. This is a result of Si-Si bond length stretching. We also observe that oxygen atoms bonded to NC surface make stronger Si-O bond than in the oxide part. These findings help us to understand relations between strain state of Si-NCs with its vibrational spectra. This provides a big advantage as the vibrational spectra of these systems can be only measured indirectly. Comparing positions of these peaks results of understanding of strain state of Si-NCs.

I'm just so relieved that it's over.
We were hanging out going nowhere,
Digging how the guitar goes,
In a song that no one knows.
James Blunt , "So long Jimmy",
Back to Bedlam, Atlantic Records/ATG, 2005.

Chapter 6

Conclusion

As the first contribution of our work atomistic simulation of NC formation in amorphous silicon-rich-oxide is accelerated through oxygen diffusion process governed by suboxide penalty energies in a Monte Carlo scheme. We observed that the available *ab initio* suboxide energies are not satisfactory for this purpose whereas one can extract them from “ideal” embedded NC suboxide densities. Even though this modification improves the sphericity of the NCs substantially, it still requires further shape constraints such as the minimization of the surface-to-volume ratio. The crystalline order, interface thickness and the strain distribution of the NC can be quantitatively analyzed with this tool. The main drawback of the algorithm is the necessity for the shape constraints which breach the predictive power of the method. The use of a multiscale approach by replacing the shape constraints with a physical law is required.

The realistic chemical environment provided by reactive force field model enables us to understand the bond topology of Si-NC/a-SiO_2 interface and its internal dynamics. Particularly, it reveals that there are different types of oxygen complexes at the Si-NC surface some of which contain three-coordinated oxygen complexes (3cO) whereas there are no double bonds. The curvature has a positive effect on the occurrence of 3cO. The relative abundance of different complexes and their charge and geometrical characteristics are extracted. The inner core is observed to be almost unstrained while the outer core and the interface region of the NC are under increasing strain up to about a few per cents. In general, our work clearly shows that the Si NC-oxide interface is more complicated than the previously proposed schemes [1, 3] which were based on solely simple bridge and double bonds. The provided information in Ch. 3 paves the way to construct realistic Monte Carlo moves for the simulation of large-scale silicon nanostructures embedded in oxide matrix. The results of bond length stretching of Si-Si bonds just under the NC surface invokes a deeper understanding of strain distribution in Si-NC.

The amorphous silica matrix applies a non-uniform strain to the Si-NC. This non uniform strain field becomes uniform in the core of the NC. The core region of the NC is observed to be under a uniform 1 % tensile strain, where both bond length and volumetric strain measures are in agreement. However, towards the NC interface, while the Si-Si bonds become more stretched, the hydrostatic and volumetric strain changes in the compressive direction. In the interpretation of the indirect strain measurements such as from spectroscopy, this dual character needs to be taken into consideration. We explain these two behaviors using the solid angle deformation of the tetrahedral-bonded Si atoms, and demonstrate that it is ultimately caused by the oxygen atoms at the interface. An equally important finding is that the overall strain profile within the Si NCs is quite nonuniform. As very recently emphasized, within the context of centrosymmetric materials, like silicon, such strain gradients locally break the inversion symmetry and may lead to profound physical consequences [55].

We introduced VACF technique as a computational tool to explore vibrational spectra of atomic systems. We studied silicon and silica as case studies. We also presented the relation between strain and vibrational spectra. Finally we introduced a novel technique called “Painted-VACF” which enables us to calculate contributions of different type of atoms to VDOS of the system. Using this tool we show the effect of surface bonds and strain fields to VDOS of system. This work provides a link between mechanical and chemical properties of Si-NC and its vibrational spectra.

The next challenge will be to construct a theory which relates strain state of

Si-NCs to its optical properties. Using charge distribution, one can calculate the Raman spectra of Si-NCs by constructing dipole correlation function. Another possible extension of this work is to study much larger NCs and obtain the size scaling trends as well as the onset of faceting from a truly microscopic model. On the technical side, the parameter development for a reactive force field still remains to be an art; further progress is required to make it more robust and versatile.

Bibliography

[1] M. Wolkin, J. Jorne, P. Fauchet, G. Allan, and C. Delerue, Phys. Rev. Lett. **82**, 197 (1999).

[2] A. Puzder, A. Williamson, J. Grossman, and G. Galli, Phys. Rev. Lett. **88** (2002).

[3] E. Luppi *et al.*, Phys. Rev. B. **75** (2007).

[4] X. H. Peng *et al.*, Phys. Rev. B. **74** (2006).

[5] T. Arguirov *et al.*, Appl. Phys. Lett. **89** (2006).

[6] H. Manasevit, I. Gergis, and A. Jones, Appl. Phys. Lett. **41**, 464 (1982).

[7] D. E. Yilmaz, C. Bulutay, and T. Cagin, J. Nanosci. Nanotech. **8**, 635 (2008), International Workshop on Nanostructured Materials (NANOMAT 2006), Antalya, TURKEY, JUN 21-23, 2006.

[8] D. E. Yilmaz, C. Bulutay, and T. Cagin, Phys. Rev. B. **77** (2008).

[9] F. Wooten, K. Winer, and D. Weaire, Phys. Rev. Lett. **54**, 1392 (1985).

[10] V. Burlakov, G. Briggs, A. Sutton, A. Bongiorno, and A. Pasquarello, Phys. Rev. Lett. **93** (2004).

[11] D. Hamann, Phys. Rev. B. **61**, 9899 (2000).

[12] P. N. Keating, Phys. Rev. **145**, 637 (1966).

[13] Y. Tu and J. Tersoff, Phys. Rev. Lett. **84**, 4393 (2000).

[14] D. Frenkel and B. Smit, *Understanding molecular simulation* (Academic Press, Inc. Orlando, FL, USA, 2001).

[15] W. Press, S. Teukolsky, B. Flannery, and W. Vetterling, *Numerical Recipes: FORTRAN* (Cambridge University Press New York, NY, USA, 1990).

[16] A. van Duin *et al.*, J. Phys. Chem. A **107**, 3803 (2003).

[17] S. Yerci *et al.*, J. Appl. Phys. **100** (2006).

[18] S. Guha, S. Qadri, R. Musket, M. Wall, and T. Shimizu-Iwayama, J. Appl. Phys. **88**, 3954 (2000).

[19] G. Hadjisavvas and P. Kelires, Phys. Rev. Lett. **93** (2004).

[20] D. Rapaport, *The art of molecular dynamics simulation* (Cambridge University Press, 2004).

[21] J. Rudnick and G. Gaspari, J. Phys. A **19**, L191 (1986).

[22] L. Canham, Appl. Phys. Lett. **57**, 1046 (1990).

[23] M. Gatti and G. Onida, Phys. Rev. B. **72** (2005).

[24] I. Vasiliev, J. Chelikowsky, and R. Martin, Phys. Rev. B. **65** (2002).

[25] O. Dictionary, Retrieved May **24**, 2004 (2004).

[26] I. Merriam-Webster, Retrieved March **2** (2005).

[27] A. Rappe and W. Goddard, WA, J. Phys. Chem. **95**, 3358 (1991).

[28] D. Brenner *et al.*, J. Phys. Cond. Mat. **14**, 783 (2002).

[29] M. De Berg, O. Cheong, and M. van Kreveld, *Computational geometry: algorithms and applications* (Springer, 2008).

[30] R. Renka, ACM Transac. on Math. Soft. **22**, 1 (1996).

[31] B. Joe, Adv. In Eng. Soft. and Workst. **13**, 325 (1991).

[32] E. Demiralp, T. Cagin, and W. Goddard, Phys. Rev. Lett. **82**, 1708 (1999).

[33] N. Huff, E. Demiralp, T. Cagin, and W. Goddard, J. Non-Cryst. Sol. **253**, 133 (1999), 18th International Congress of Glass, SAN FRANCISCO, CALIFORNIA, JUL 05-10, 1998.

[34] H. Hofmeister, F. Huisken, and B. Kohn, E. Phys. J. D **9**, 137 (1999), 9th International Symposium of Small Particles and Inorganic Clusters, LAUSANNE, SWITZERLAND, SEP 01-05, 1998.

[35] P. Kroll and H. Schulte, Phys. Stat. Sol. B **243**, R47 (2006).

[36] P. Kroll, Computation of temperature-pressure phase diagrams of high-pressure nitrides, in *Materials Research at High Pressure*, edited by Manaa, MR and Goncharov, AF and Hemley, RJ and Bini, R, , MATERIALS RESEARCH SOCIETY SYMPOSIUM PROCEEDINGS Vol. 987, pp. 11–16, 2007, Symposium on Materials Research at High Pressure held at the 2006 MRS Fall Meeting, Boston, MA, NOV 27-28, 2006.

[37] A. Pasquarello, M. Hybertsen, and R. Car, Nature **396**, 58 (1998).

[38] M. Boero, A. Oshiyama, P. Silvestrelli, and K. Murakami, Appl. Phys. Lett. **86** (2005).

[39] V. Kumar, *Nanosilicon* (Elsevier Science, 2008).

[40] R. People *et al.*, Appl. Phys. Lett. **45**, 1231 (1984).

[41] D. Lyons, K. Ryan, M. Morris, and J. Holmes, Nano Lett. **2**, 811 (2002).

[42] K. Hong, J. Kim, S. Lee, and J. Shin, Nano Letters **8**, 1335 (2008).

[43] A. Thean and J. Leburton, Appl. Phys. Lett. **79**, 1030 (2001).

[44] A. M. Smith, A. M. Mohs, and S. Nie, Nature Nanotech. **4**, 56 (2009).

[45] H. Coffin *et al.*, J. Appl. Phys. **99** (2006).

[46] M. Ippolito, S. Meloni, and L. Colombo, Appl. Phys. Lett. **93** (2008).

[47] P. Chou and N. Pagano, *Elasticity: tensor, dyadic, and engineering approaches* (Courier Dover Publications, 1992).

[48] P. M. Gullett, M. F. Horstemeyer, M. I. Baskes, and H. Fang, Mod. Sim. Mat. Sci. Eng. **16** (2008).

[49] C. Pryor, J. Kim, L. Wang, A. Williamson, and A. Zunger, J. Appl. Phys. **83**, 2548 (1998).

[50] W. Curtin and R. Miller, Mod. Simul. Mat. Sci. Eng. **11**, R33 (2003).

[51] N. Bernstein *et al.*, Phys. Rev. B. **62**, 4477 (2000).

[52] M. Cardona, G. Güntherodt, and R. Merlin, *Light scattering in solids* (Springer, 2007).

[53] J. M. Carpenter and D. L. Price, Phys. Rev. Lett. **54**, 441 (1985).

[54] D. E. Yilmaz, C. Bulutay, and T. Cagin, Appl. Phys. Lett. **94**, 191914 (2009).

[55] M. S. Majdoub, P. Sharma, and T. Cagin, Phys. Rev. B. **78**, 121407 (2008).